

BEAM MODULATION IN DOUBLE GAP VIRTUAL CATHODE
OSCILLATOR

A THESIS SUBMITTED TO
THE GRADUATE SCHOOL OF NATURAL AND APPLIED SCIENCES
OF
MIDDLE EAST TECHNICAL UNIVERSITY

İBRAHİM SEMİH KÜÇÜK

IN PARTIAL FULFILLMENT OF THE REQUIREMENTS
FOR
THE DEGREE OF MASTER OF SCIENCE
IN
ELECTRICAL AND ELECTRONICS ENG.

SEPTEMBER 2018

Approval of the thesis:

**BEAM MODULATION IN DOUBLE GAP VIRTUAL CATHODE
OSCILLATOR**

submitted by **İBRAHİM SEMİH KÜÇÜK** in partial fulfillment of the requirements for the degree of **Master of Science in Electrical and Electronics Eng. Department, Middle East Technical University** by,

Prof. Dr. Halil Kalıpçılar _____
Dean, Graduate School of **Natural and Applied Sciences**

Prof. Dr. Tolga Çiloğlu _____
Head of Department, **Electrical and Electronics Eng.**

Prof. Dr. Şimşek Demir _____
Supervisor, **Electrical and Electronics Eng. Dept., METU**

Examining Committee Members:

Prof. Dr. Sencer Koç _____
Electrical and Electronics Engineering Department, METU

Prof. Dr. Şimşek Demir _____
Electrical and Electronics Engineering Department, METU

Assoc. Prof. Dr. Serhat Çakır _____
Physics Department, METU

Prof. Dr. Asım Egemen Yılmaz _____
Electrical and Electronics Eng. Dept., Ankara University

Assist. Prof. Dr. Mehmet Ünlü _____
Electrical and Electronics Eng. Dept., TOBB ETU

Date: _____

I hereby declare that all information in this document has been obtained and presented in accordance with academic rules and ethical conduct. I also declare that, as required by these rules and conduct, I have fully cited and referenced all material and results that are not original to this work.

Name, Last Name: İBRAHİM SEMİH KÜÇÜK

Signature :

ABSTRACT

BEAM MODULATION IN DOUBLE GAP VIRTUAL CATHODE OSCILLATOR

KÜÇÜK, İBRAHİM SEMİH

M.S., Department of Electrical and Electronics Eng.

Supervisor : Prof. Dr. Şimşek Demir

September 2018, 84 pages

Viricator is a promising high power microwave device when its simplicity, frequency tunability, lack of external magnetic field source are considered. Viricator gains importance especially susceptibility testing to electromagnetic pulses of electronic equipments with its tunability. Apart from advantages, main bottleneck of the viricator is its low efficiency. Tunability and efficiency enhancement studies are still continued in literature. Double gap viricator draws attention due to its tunability, generation frequency stability and microwave radiation efficiency result from beam modulation. This thesis examines double gap viricator in terms of tunability under external signal injection, effect of both plungers and coupling window on output electromagnetic power. With signal injection, efficiency increase, due to earlier start time, is obtained and frequency locking behavior of viricator is observed. For the various configurations of plungers, theoretical cavity field distributions are analyzed and it is obtained that efficiency is maximized when field distribution on beam center is at maximum. Tuning

procedure for double gap vircator is developed and its applicability for different AK gap distances and gap voltages are shown.

Keywords: Beam modulation, double anode, double gap, virtual cathode oscillator

ÖZ

ÇİFT AÇIKLIKLI SANAL KATOT OSİLATÖRÜNDE ELEKTRON DEMET MODULASYONU

KÜÇÜK, İBRAHİM SEMİH

Yüksek Lisans, Elektrik Elektronik Mühendisliği Bölümü

Tez Yöneticisi : Prof. Dr. Şimşek Demir

Eylül 2018 , 84 sayfa

Basitliği, frekans ayarlanabilirliği, dışarıdan uygulanan bir manyetik alana ihtiyaç duymaması bakımından virkatör dikkat çeken bir yüksek güçlü mikrodalga cihazıdır. Frekans ayarlanabilirliği, elektronik cihazların elektromanyetik darbelere dayanım testlerinde virkatöre önem kazandırmaktadır. Bunların yanısıra, esas olumsuz özelliği ise verim düşüklüğüdür. Verim düşüklüğünü gidermeye ve frekans ayarlanabilirliğini artırmaya dönük çalışmaların literatürde devam ettiği görülmektedir. Çift açıklıklı virkatör ise frekans ayarlanabilirliği, frekans istikrarı ve elektron demet modülasyonundan kaynaklanan mikrodalga verimliliği ile dikkat çekmektedir. Bu tezde çift açıklıklı virkatör dışardan uygulanan sinyal altında frekans ayarlanabilirliği, piston ve bağlaşım penceresinin çıkış EM gücüne etkisi bakımından incelenmiştir. Sinyal sağlama ile, erken mikrodalga salınımından dolayı verim artışı ve frekans kilitlenme davranışı gözlenmiştir. Pistonların farklı konumları için, teorik kovuk elektrik alan dağılımları incelenmiş ve elektrik

alan dađılımlının elektron demet merkezinde en yüksek deęeri alması durumunda verim artışının tepe yaptığı görülmüştür. Bu virkatör yapısı için frekans ayar adımları geliştirilmiş ve farklı AK açıklıkları ve açıklık gerilimleri için uygulanabilirliği gösterilmiştir.

Anahtar Kelimeler: elektron demet modülasyonu, çift anot, çift açıklık, sanal katot osilatörü

To my family

ACKNOWLEDGMENTS

In the first place, I would like to express my gratitude to Prof. Dr. Şimşek Demir for his guidance, support and encouragement during my thesis.

I also thank to my colleague and friend Büşra Timur for her contributions to my thesis.

Many thanks to members of ARC304 Enis Kobal, Yiğit Haykır and Cihan Aşçı for their friendship.

There is very special someone whose friendship is not affected with distance and time. I would like to thank to my oldest friend Mehmet Yavuz.

Special thanks for Ahmet Erol, Eren Aydın, Hüseyin Boyacı and Hilal Kübra Dumanlı Aydın for their warm friendship. It is priceless for me to know that they are with me whenever I need them. Life is much more beautiful with them.

I would like to thank my cousin Ahmet Sarnıç for sharing both my joy and trouble.

Thanks to my aunt Gülnur Bağana for being with me at the every cornerstone of my life.

I cannot present enough thanks to my parents and my brother. I dedicated this thesis to my family, most important people in my life.

Last thanks are for my grandmother and grandfather for caring me so much during my entire life.

TABLE OF CONTENTS

ABSTRACT	v
ÖZ	vii
ACKNOWLEDGMENTS	x
TABLE OF CONTENTS	xi
LIST OF TABLES	xiv
LIST OF FIGURES	xvi
LIST OF ABBREVIATIONS	xx
CHAPTERS	
1 INTRODUCTION	1
2 VIRTUAL CATHODE OSCILLATOR	5
2.1 System Point of View	5
2.2 Virtual Cathode Oscillator	6
2.2.1 Explosive Emission Process and Plasma Formation	7
2.2.2 Space Charge Limiting Current	9
2.2.2.1 Child-Langmuir Law	9

	2.2.2.2	Relativistic Solution of 1D Space Charge Limiting Current	12
	2.2.3	Virtual Cathode Formation and Radiation Mechanism	13
	2.2.4	Double Gap Vircator	15
	2.2.4.1	Literature Research of Double Anode Vircators	16
	2.2.5	Effect of External Signal	22
	2.2.6	Axial Vircator with Feedback Structures	22
	2.2.6.1	Feedback Annuluses	23
	2.2.6.2	Reflectors	25
3		VIRCATOR SIMULATION ENVIRONMENT : MAGIC TOOL SUITE	27
	3.1	Applying of Pulse Voltage Waveform	31
	3.1.1	Usage of Circuit Option in Port Command	32
	3.2	Anode Modeling	33
	3.2.1	Fraction Model	35
	3.2.2	Grid Model	37
	3.3	Mode Distribution in Magic	40
	3.4	Data Filtering	41
4		DOUBLE GAP VIRCATOR SIMULATION RESULTS	43
	4.1	Field Injection	47
	4.1.1	Feedback Disable	49

4.1.1.1	Frequency Shifts	51
4.1.1.1.1	S Band Frequency Locking	53
4.1.1.2	Injection Input Phase Delay	54
4.1.1.3	Cavity Field Distribution	54
4.1.2	Feedback Enable	57
4.2	Coupling Window	57
4.3	Small Plunger	58
4.4	Large Plunger	60
4.4.1	Constant Cavity Length	61
4.5	Foil Transmission Fraction	63
4.6	Natural Oscillation Frequencies and Tuning Procedure .	64
4.6.1	Tuning to 2.56GHz in Main Geometry	66
4.6.2	Tuning Procedure for 750kV Peak Input Voltage	67
4.6.3	Tuning Procedure for Different AK Gap Distances	69
4.6.3.1	11mm AK Gap Distance	69
4.6.3.2	12m AK Gap Distance	69
4.6.3.3	13m AK Gap Distance	70
5	CONCLUSION AND FUTURE WORK	73
	REFERENCES	77

LIST OF TABLES

TABLES

Table 3.1	Mean input voltages on the flat region of waveform	33
Table 3.2	Effect of material on foil behavior	40
Table 3.3	Effect of geometrical opening on foil behavior	41
Table 4.1	Input parameters for injected field power without feedback . .	49
Table 4.2	Results for varying injected field power without feedback . . .	50
Table 4.3	Input parameters for field injection with different frequencies without feedback	52
Table 4.4	Results for field injection with different frequencies without feedback	52
Table 4.5	Input parameters for S band field injection with different fre- quencies without feedback	53
Table 4.6	Results for field injection for constant cavity length without feedback	56
Table 4.7	Results for varying injected field with feedback	57
Table 4.8	Input parameters for small plunger shift cases	58
Table 4.9	Results for small plunger shift cases	60
Table 4.10	Results for position of large plunger shift cases	61

Table 4.11 Results for constant cavity length with feedback	62
Table 4.12 Results for different foil transmission fraction values	63
Table 4.13 Results for tuning procedure to main geometry	66
Table 4.14 Inputs for 750kV for application	67
Table 4.15 Results for 750kV application	67
Table 4.16 Results after tuning procedure for 750 kV	68
Table 4.17 Results for 11mm AK gap	69
Table 4.18 Best result after tuning procedure for 11mm AK gap case . .	69
Table 4.19 Results for 12mm AK gap	70
Table 4.20 Best result after tuning procedure for 12mm AK gap case . .	70
Table 4.21 Results for 13mm AK gap	70
Table 4.22 Best result after tuning procedure for 13mm AK gap case . .	71

LIST OF FIGURES

FIGURES

Figure 2.1	High power microwave system diagram	5
Figure 2.2	Virtual cathode devices (a)axial vircator (b)reflex triode (c)reditron (d)coaxial vircator (d) double gap vircator with feedback window (e) 3 cavity axial vircator. Arrow indicates the microwave radiation direction.	7
Figure 2.3	Microscopic view of the whisker in the cathode surface	8
Figure 2.4	1D Planar Diode	10
Figure 2.5	Phase Space Plot of Axial Vircator	14
Figure 2.6	Axial vircator with reflectors presented in Ref. [1]	26
Figure 3.1	The processing cycle [2]	28
Figure 3.2	Leapfrog time integration scheme [2]	29
Figure 3.3	(a)Yee cell [3] (b)Location of electric and magnetic fields in half and full grid cells [3]	30
Figure 3.4	Coaxial shape of input	31
Figure 3.5	Input signal of the axial vircator for different excitation	32
Figure 3.6	Coaxial test geometry for port circuit	33
Figure 3.7	Signal excitation to coaxial structure with port circuit	34

Figure 3.8 Magic input Signal of the axial vircator for different port circuit time constant	34
Figure 3.9 Phase space for the foil test at (a)1.459ns (b)1.647ns (c)2.898ns (d)4.42ns	36
Figure 3.10 Electron ratios for 0.6 foil transmission fraction value with respect to beam energy and foil thicknesses. (a)Undelected electron ratio vs. Beam energy (b)Forward scattering electron ratio vs. Beam energy	37
Figure 3.11 Magic foil grid model	38
Figure 3.12 Grid models in Magic for (a)cylindrical and (b) cartesian coordinate system	38
Figure 3.13 Phase space for the foil test at (a)2.155ns (b)2.732ns (c)3.925ns (d)6.195ns	39
Figure 3.14 Magic field measurement points for mode analysis in (a)cylindrical waveguide (b)rectangular waveguide	40
Figure 3.15 TM_{01} mode distribution of (a)electric field intensity (b) magnetic flux density	42
Figure 4.1 Double gap vircator	43
Figure 4.2 P_y vs. y phase space of double gap vircator (a)6.017ns (b)6.104ns (c)6.191ns (d)6.278ns	44
Figure 4.3 Microwave spectrum at the output of the device	44
Figure 4.4 Field distribution at the modulating cavity	45
Figure 4.5 Field distribution at the output	45
Figure 4.6 \bar{E} field distribution on modulating cavity	46
Figure 4.7 E_y at the midplane of vircator	46

Figure 4.8 \bar{E}_y field variation in time at modulating cavity	47
Figure 4.9 Cross sections of the modulating cavity under TE_{10} mode injection (a)longitudinal (b)transverse	48
Figure 4.10 Vircator x-y cut with field injection port	49
Figure 4.11 (a)Spectrum of generated EM fields (b)Output microwave power (filtered by step filter with a period of generated wave)	51
Figure 4.12 TE_{106} mode distributions on the beam center	51
Figure 4.13 Output spectrum of generated electromagnetic fields	52
Figure 4.14 TE_{103} mode distributions on the beam center	53
Figure 4.15 (a)Output spectrum of generated electromagnetic fields (b)Output spectrum of generated electromagnetic fields	54
Figure 4.16 (a)Time delayed injected signals (b)Output signals	55
Figure 4.17 (a)Geometry for cavity field distribution test under external field (b) Vircator x-y cut with enabling feedback	55
Figure 4.18 (a)Cavity field distributions (b) Output spectrum	56
Figure 4.19 (a) Spectrum of generated EM fields (b) Output microwave power (filtered by step filter with a period of generated wave)	58
Figure 4.20 Main geometry of double gap vircator	58
Figure 4.21 (a)Peak power efficiency vs. coupling window (b)Energy efficiency vs. coupling window	59
Figure 4.22 Efficiency vs position of small plunge (a)Peak power efficiency (b)Energy efficiency	59
Figure 4.23 Field distribution around beam center	61
Figure 4.24 Resonant mode field distribution in modulating cavity	62

Figure 4.25 (a)Output power (filtered by step filter with period of generated wave) (b) electromagnetic spectrum of outgoing field	64
Figure 4.26 Tuning geometry used for finding natural oscillation frequencies	64
Figure 4.27 Electromagnetic spectrum of outgoing field	65
Figure 4.28 Output spectrum for 2.56GHz tuning procedure	66
Figure 4.29 (a)Output spectrum for main structure (b)Output spectrum shows natural oscillation frequencies	67
Figure 4.30 Field distribution for 750kV application	68

LIST OF ABBREVIATIONS

AA	Anode-anode
AK	Anode-cathode
CST	Computer Simulation Technology
FDTD	Finite Difference Time Domain
EM	Electromagnetic
FOI	Swedish Defense Research Agency
FTF	Foil Transmission Fraction
FWHM	Full Width Half Maximum
HPM	High Power Microwave
ISL	French-German Research Institute of Saint-Louis
ITS	Integrated Tiger Series
LTD	Linear Transformer Device
METU	Middle East Technical University
PIC	Particle-in-Cell
RF	Radio Frequency
SHF	Super High Frequency
TEM	Transverse Electromagnetic
VC	Virtual Cathode
VCA	Virtual Cathode Amplifier
Vircator	Virtual Cathode Oscillator

CHAPTER 1

INTRODUCTION

Virtual cathode oscillators (vircators) are the device which converts high voltage pulses to high power microwaves (HPM). Microwave generation in vircator is based on bremsstrahlung radiation mechanism which results from the acceleration of the electrons in the electric or magnetic field. Vircator works under vacuum therefore it can handle GW level powers which is also the main advantage of the high power microwave vacuum devices over conventional microwave devices and solid state devices. When high voltage is applied to cathode, electrons are emitted by explosive emission process, accelerated under electric field and pass through transparent anode. When the beam current exceeds the local space-charge limiting current of the enclosing geometry beyond anode region, virtual cathode (VC) forms and partial transmission and partial reflection of electron beam is observed. Microwave is generated by two oscillation processes namely, reflexing oscillations of electrons and virtual cathode oscillation which both start after VC formation. The main advantage of this device is that externally applied magnetic field is not required for HPM generation. Besides, it does not have components like slow wave structure which makes manufacturing process more complicated. Lack of external coils or magnets and complex structures makes it compact and simple. Simplicity leads to another advantage of easy maintenance. Various studies show the frequency tunability is achievable for vircator structures [4, 5, 6, 7, 8] and this advantage makes the device a good option in susceptibility measurements of electronic devices to EM pulses [9]. Phase locking of the vircators enables driven of them by other HPM sources [10, 11, 12, 13] and locking of vircators to each other and even using them as

phased array antennas [13, 14, 15, 16, 17]. The main disadvantage of the vircator is its low efficiency. There are numerous studies that aim to increase beam to microwave efficiency of the device, including adding reflectors, feedback annulus, using cavity structures etc [1, 18, 19, 20, 21]. Another disadvantage is the gap closure due to anode and cathode plasma expansions. Due to gap closure, emission current is increased then frequency chirps upwards and eventually pulse is shortened. Since intense electron beams are employed in the devices, it directly affects the lifetime of the cathode and anode materials. In order to overcome gap closure and to enhance limited lifetimes of materials and microwave generation efficiency, different anode and cathode materials with etching and coating processes were tested in literature [22, 23, 24, 25, 26, 27]. As another drawback, efficiency can be limited by competition between various modes.

Double gap vircator is a promising device when its radiation frequency stability during pulse and possibility of frequency arrangement by mechanically adjusting plungers are considered [28]. 15% frequency tunability was experimentally demonstrated by simultaneously varying both plungers of the system [29]. Premodulation of the electron beam occurs in this device due to feedback via coupling window [30]. Because of this feedback to the beam, conversion efficiency of the device is stated to be enhanced more than three times higher than the one has a single gap with similar conditions [6, 29]. The aim of this thesis is to numerically examine double gap virtual cathode oscillator together with the effects of plungers in order to achieve frequency tuning of the device for different operating conditions. Simulations are conducted in Magic Tool Suite which is Finite Difference Time Domain (FDTD) Electromagnetic (EM) Particle in Cell (PIC) code. Magic 3D is commonly used code in simulations of HPM devices. In the numerical analysis of the device, coupling fields of the cavity are mimicked by the externally applying electric field. Under this application, effect of beam modulation is understood and cavity field distribution condition, which satisfies when standing wave maximum of cavity fields is in the beam center, is observed. In addition, frequency and phase locking behavior of the device to injected signal are shown. Moreover, effect of plungers on efficiency due to cavity field distribution is observed. Besides, length of the coupling window is

found to be sensitive parameter that can satisfies required feedback to cavity for efficient usage of device. After observation of effects of the plungers and coupling window, frequency tuning procedure for the device is proposed and tested with different AK gap voltages and AK gap distances.

In the next chapter, explosive emission process and plasma formation in vircator structures are explained. Besides, 1D space charge limiting current for both nonrelativistic and relativistic cases are derived and radiation mechanism of vircator is described. Also, literature research for double gap vircator, axial vircator with feedback structures of annuluses and reflectors are given. Chapter III start with a brief explanation of Magic Tool Suite algorithm. For the usage of Magic in vircator simulations, excitation of high voltage signal to vircator, anode modelling with fraction and grid option, mode analysis of the generated signal and filtering of output data externally are also given in the same chapter. Chapter IV is consisting of simulation results of the double gap vircator structure which includes the external signal injection, frequency and phase locking, effect of plungers and foil transmission fraction parameter and tuning procedure. Lastly, Chapter V gives a conclusion and future work of this thesis study.

CHAPTER 2

VIRTUAL CATHODE OSCILLATOR

2.1 System Point of View

Generally, vircators are used as a microwave generator component of the high power microwave systems shown in Figure 2.1. In this system, prime power



Figure 2.1: High power microwave system diagram

subsystem outputs low power continuously or for a long pulse to next block of pulsed power. Pulsed power subsystem stores the energy given by prime power and discharges this energy in a short time of interval onto microwave source. For some cases, pulsed forming network can be used in between pulsed power and microwave source subsystems in order to obtain desired pulse shape for the next block. Microwave source converts the pulsed energy into electromagnetic (EM) pulse wave. According to mode of EM wave produced by microwave source, mode converter might be required for getting effective radiation pattern. Antenna is the last subsystem and its usage is the radiation of high power microwave onto target [9]. All of the subsystems beginning from the pulsed power should be under vacuum in order to prevent electrical breakdown in the system.

2.2 Virtual Cathode Oscillator

Figure 2.2a is called as axial vircator and it is the most basic vircator type. This structure consists of a cathode, an anode and drift tube enclosing them. In this device, emitted electrons from cathode are accelerated to anode under high potential difference between cathode and anode. Anode behaves as a short circuit to electromagnetic wave and transparent to electron beam. It could have either grid type which has geometrical transparency or thin foil. In both types, high transparency to the electron beam is aimed. The device is operated based on the phenomena of space-charge limiting current and virtual cathode (VC) formation. When injected beam current to the drift tube exceed the space-charge limiting current of the tube, VC forms and electron reflexing process starts. VC oscillations and electron reflexing oscillation between cathode and VC due to this phenomena are the sources of the microwave generation. Commonly, negative pulse voltage is applied to cathode and anode is grounded. However, in reflex triode shown in Figure 2.2b positive pulse voltage is applied to anode while cathode is grounded. Figure 2.2c shows the reditron configuration which is developed to prevent radiation results from reflexing motion of electrons by using axial magnetic field and thick anode with slit opening. Figure 2.2d belongs to coaxial vircator. Electrons are emitted from a cylindrical cathode and accelerated through a transparent cylindrical anode. Since the electron motion is radial, no power loss due to axially escaping electron through drift tube is observed. Besides, it enables feedback from microwave generation region to AK gap due to opening. It has also enhanced life time of materials due to lower beam current density which results from increased area of the cylindrical cathode. Apart from the advantages of coaxial configuration, it has lack of tunability, alignment and configuration optimization difficulties and mode competition between TE_{11} and TM_{01} modes [9]. Figure 2.2e shows the double anode configuration with internal feedback mechanism. This structure is also the subject of this thesis. Stability and tunability of frequency of generation due to feedback from the generation region to cavity between anodes are the main advantages of this device. Figure 2.2f is the axial vircator with three cavity device proposed by Ref. [19].

Three annuluses in the figure can be considered as microwave filter and it gives feedback towards the anode-VC region to enhance beam rf interaction [31].

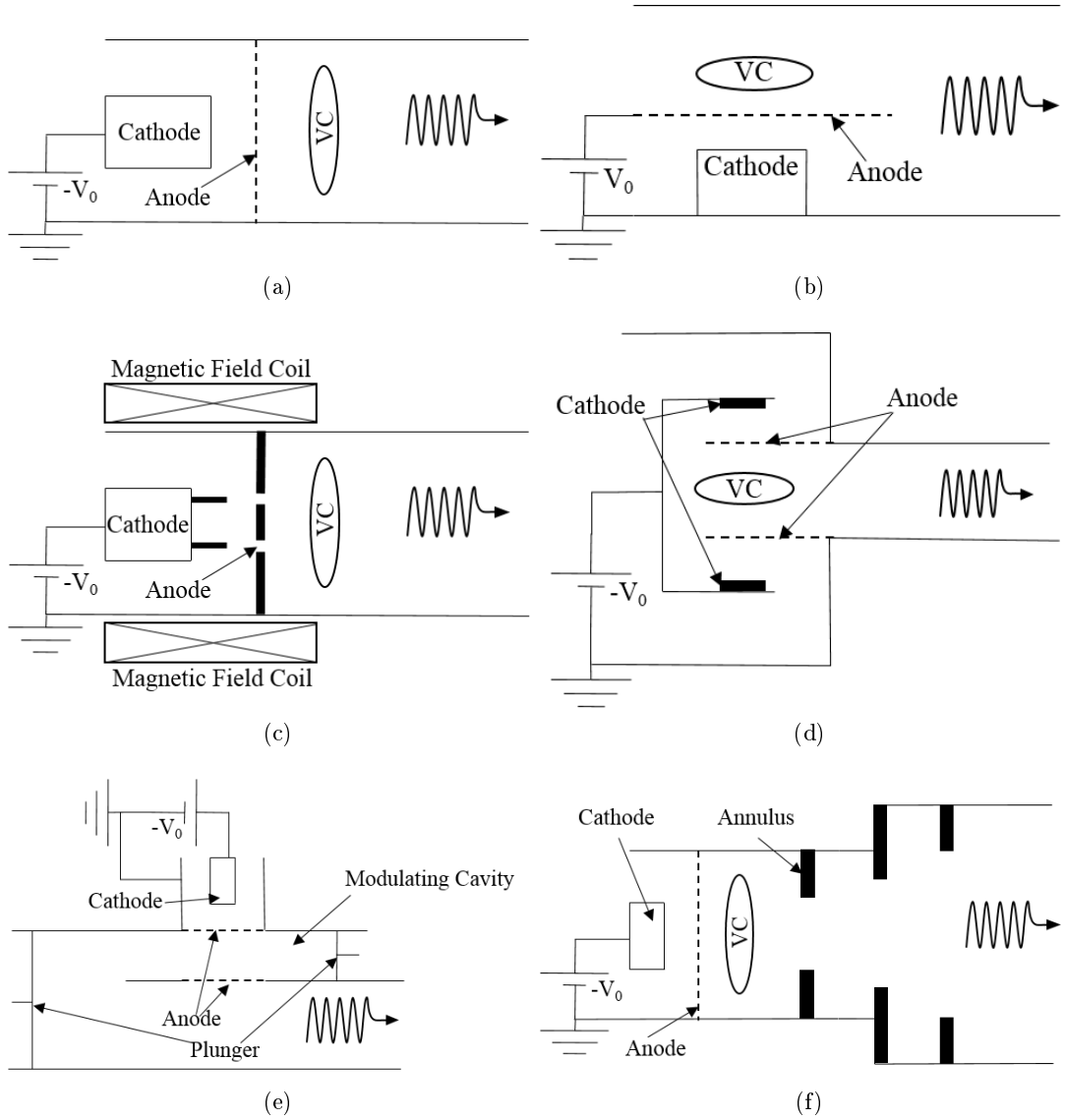


Figure 2.2: Virtual cathode devices (a)axial vircator (b)reflex triode (c)reditron (d)coaxial vircator (d) double gap vircator with feedback window (e) 3 cavity axial vircator. Arrow indicates the microwave radiation direction.

2.2.1 Explosive Emission Process and Plasma Formation

Almost every surface consists of impurities called whiskers shown in Figure 2.3. These whiskers dimensions are typically 10^{-4} cm in height and less than 10^{-5} cm in radius [32]. When the electric field is applied between anode and cathode, field

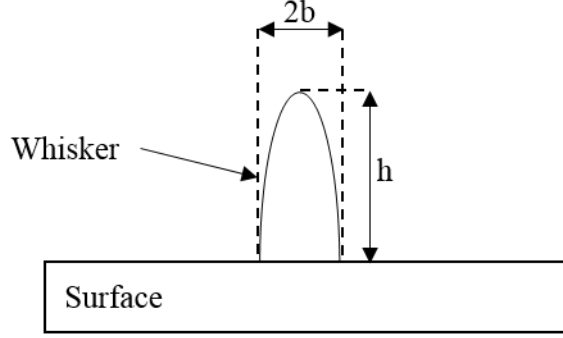


Figure 2.3: Microscopic view of the whisker in the cathode surface

at the whisker tips is increased by the amount of the electric field enhancement factor , f :

$$E_{tip} = fE \quad (2.1)$$

where E_{tip} is the electric field at the tip of the whisker and E is the macroscopic electric field. Field enhancement factor is given as [33, 34]:

$$f = \frac{(\lambda^2 - 1)^{1.5}}{\lambda \ln(\lambda + \sqrt{\lambda^2 - 1}) - \sqrt{\lambda^2 - 1}} \quad (2.2)$$

where, λ is the ratio of height of whisker to its radius. Because of this factor, electric field at the tip is increased by several hundreds over the macroscopically applied electric field [33, 34]. For the given whisker dimensions above, formula in Equation 2.2 gives 79.8. In the initial phase of applying electric field to diode, field emission process takes place [34]. In this phase, required electric field value for the field emission process is reached due to field enhancement factor at the tips of the whisker even if the macroscopic electric field does not satisfy the required value. Once the field emission process starts, temperature is increased excessively due to Joule heating. This rise in temperature leads to evaporation of the whisker to a vapor state. This state quickly ionizes and creates plasma burst (i.e., plasma flares) for each whisker. Every plasma flares expand and merge with other flares to form uniform plasma sheet over the cathode surface[33, 34, 35]. Thus, this surface can be considered as the source of unlimited flux of electron source with zero work function [32]. Electron emission from the cathode plasma is limited by the space-charge limiting current [33, 34].

Anode plasma is formed due to electron bombardment to the anode surface [4, 36, 37, 38]. In Ref. [36], it is said that plasma formation at anode due

to electron striking is considered as complicated process. Moreover, it is also indicated that this process is not fully understood yet. In the same paper, two possible plasma formation process is added. The first one is the melting and evaporation of the anode surface and the second one is electron stimulated desorption of the contaminants on the anode surface. In Ref. [37], impurities such as water and oils adhered or absorbed on the anode surface are thought as the source of the anode plasma. In the same study, anode temperature is estimated as $130^{\circ}C$ at the onset of anode plasma which was $30ns$ while cathode plasma forms immediately after the rise of beam current. It is indicated that the temperature of anode is below the melting point of aluminum anode material however it is high enough to evaporate impurities such as water or oil on the surface of anode.

2.2.2 Space Charge Limiting Current

Beam self generated fields result in limit in the beam transport in longitudinal and transversal direction [35]. Scope of this part is the only longitudinal limit. In vircators, virtual cathode (i.e., potential well [39]) is formed when the beam current exceeds the local space-charge limiting current. After this point, some of the electrons are reflected back to the anode and oscillation process of VC and reflex electrons start.

2.2.2.1 Child-Langmuir Law

Child-Langmuir Law is published by Child [40] and Langmuir [41] and it gives the limiting current in one dimensional diode structure consisting of cathode and anode given in Figure 2.4. Derivation steps in [9] are followed in this part. Following assumptions are made for the derivation.

- Diode in Figure 2.4 extends infinitely along the dashed lines provides that no fringing fields exist.
- No time dependence exists.

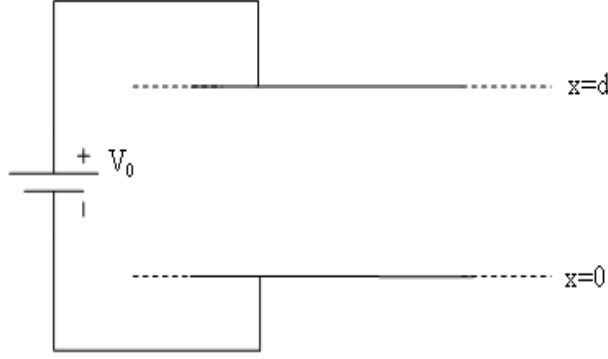


Figure 2.4: 1D Planar Diode

- No ion current exists.
- Particle motion is nonrelativistic i.e. $V_0 < 500kV$.
- No defocusing self fields exists.
- Source can supply infinite amount of electron flux.
- Continuous particle flow exist.
- Initial electron velocity is zero.

Under these assumptions, start with Poisson equation which is given in Equation 2.3:

$$\nabla^2 \phi(x) = -\frac{\rho}{\epsilon_0} = \frac{en(x)}{\epsilon_0} \quad (2.3)$$

where e , $n(x)$, ρ , $\phi(x)$ and ϵ are electron charge, number density of electrons, charge density, electric potential and permittivity respectively. Then, use equation of continuity given in Equation 2.4.

$$\bar{\nabla} \cdot \bar{J} = -\frac{\partial \rho}{\partial t} = 0 \quad (2.4)$$

$$\frac{dJ}{dx} = 0 \quad (2.5)$$

where J is current density. Right hand side of Equation 2.4 is equal to zero due to time independency assumption which means that current between the plates is constant. Electric current density between plates is $\bar{J} = -en(x)v_x(x)\hat{a}_x$ where

$v_x(x)$ is electron velocity. Substitute electric current density expression into Equation 2.3.

$$\nabla^2\phi(x) = \frac{J}{\epsilon_0 v_x(x)} \quad (2.6)$$

Now, apply conservation of energy for nonrelativistic particles, which can be shown in Equation 2.7 into Equation 2.6. Then, Equation 2.8 can be obtained.

$$\frac{1}{2}m_e v_x(x)^2 = e\phi(x) \quad (2.7)$$

where m_e is mass of electron.

$$\frac{d^2\phi}{dx^2} = \sqrt{\frac{m_e}{2e}} \frac{J}{\epsilon_0 \phi^{1/2}} \quad (2.8)$$

Let us call $A = \sqrt{\frac{m_e}{2e}} \frac{J}{\epsilon_0}$ and $\phi' = \frac{d\phi}{dx}$.

$$\frac{d\phi'}{dx} = A\phi^{-1/2} \quad (2.9)$$

Substitute $dx = \frac{d\phi}{\phi'}$ into Equation 2.9.

$$\phi' d\phi' = A\phi^{-1/2} d\phi \quad (2.10)$$

Integrate both sides from $x = 0$ to x by applying the boundary condition of zero electric field at cathode surface i.e., $\left. \frac{d\phi}{dx} \right|_{x=0} = -E \Big|_{x=0} = 0$. At this condition, diode region pass through space charge limited flow from source limited flow [35].

$$\frac{\phi'^2}{2} = 2A\phi^{1/2} \quad (2.11)$$

Equation 2.12 can be obtained by taking the square root of Equation 2.11.

$$\phi' = 2\sqrt{A}\phi^{1/4} \quad (2.12)$$

Substitute $\frac{d\phi}{dx} = \phi'$ into Equation 2.12.

$$\phi^{-1/4} d\phi = 2\sqrt{A} dx \quad (2.13)$$

By integrating both sides from $x = 0$ to $x = d$ then taking the square of the results, Equation 2.14. is obtained.

$$J = \frac{4\epsilon_0}{9} \sqrt{\frac{2e}{m_e}} \frac{\phi^{3/2}}{d^2} \quad (2.14)$$

Equation 2.14 is the space charge limiting current for 1D diode structure.

2.2.2.2 Relativistic Solution of 1D Space Charge Limiting Current

Relativistic solution of 1D space charge limited diode is introduced by Jory and Trivelpiece [42]. Starting with substituting $J = -\rho v$ into Poisson equation in Equation 2.3, Equation 2.15 can be obtained.

$$\frac{d\phi^2}{dx^2} = \frac{J}{\epsilon_0 v} \quad (2.15)$$

Unknown v in terms of relativistic factor, γ , can be found from $\gamma = \frac{1}{\sqrt{1-\frac{v^2}{c^2}}}$ as in Equation 2.16.

$$v = c \frac{\sqrt{\gamma^2 - 1}}{\gamma} \quad (2.16)$$

where c is speed of light. Conservation of energy can be written as in Equation 2.17.

$$(\gamma - 1)m_0c^2 = e\phi \quad (2.17)$$

Define normalized potential U as $\frac{e\phi}{m_0c^2}$. From Equation 2.17, γ is equal to Equation 2.18.

$$\gamma = 1 + \frac{e\phi}{m_0c^2} = 1 + U \quad (2.18)$$

Equation 2.19 can be found by substituting Equation 2.18 into Equation 2.16

$$v = c \frac{\sqrt{U(U+2)}}{1+U} \quad (2.19)$$

Substitute Equation 2.19 into Equation 2.15 in order to find Equation 2.20.

$$\frac{m_0c^2}{e} \frac{d^2U}{dx^2} = \frac{J}{\epsilon_0 c} \frac{1+U}{\sqrt{U(U+2)}} \quad (2.20)$$

Equation 2.20 is reorganized and K is defined as indicated Equation 2.21.

$$\frac{d^2U}{dx^2} = \frac{eJ}{\epsilon_0 m_0 c^3} \frac{1+U}{\sqrt{U(U+2)}} = K \frac{1+U}{\sqrt{U(U+2)}} \quad (2.21)$$

By defining $U' = \frac{dU}{dx}$ and substituting $dx = \frac{dU}{U'}$ into Equation 2.21, Equation 2.22 can be obtained.

$$U' dU' = K \frac{1+U}{\sqrt{U(U+2)}} dU \quad (2.22)$$

$$\int_{x=0}^x U' dU' = \int_{x=0}^x K \frac{1+U}{\sqrt{U(U+2)}} dU \quad (2.23)$$

Integration of Equation 2.23 with the condition of $\frac{dU}{dx}\Big|_{x=0} = 0$ gives Equation 2.24. This implies that electric field at cathode is zero which is the condition of space charge limited emission.

$$\frac{U'2}{2} = K\sqrt{U(U+2)} \quad (2.24)$$

Taking the square root of Equation 2.24 gives Equation 2.25

$$\frac{dU}{dx} = \sqrt{2K\sqrt{U(U+2)}} \quad (2.25)$$

Substitute Equation 2.18 into Equation 2.25.

$$\frac{d\gamma}{dx} = \sqrt{2K}(\gamma^2 - 1)^{1/4} \quad (2.26)$$

Equation 2.27 can be found by reorganizing Equation 2.26.

$$d\gamma(\gamma^2 - 1)^{-1/4} = \sqrt{2K}dx \quad (2.27)$$

For $U > 1$, left hand side of the Equation 2.27 can be expanded in binomial series. Then it is integrated term by term. By taking only the first term in series, Equation 2.28 is reached.

$$\gamma \approx \left[\sqrt{\frac{K}{2}}x + 0.8471 \right]^2 = \left[\sqrt{\frac{eJ}{2\epsilon_0 m_0 c^3}}x + 0.8471 \right]^2 \quad (2.28)$$

The constant term is said to be selected to satisfy the boundary condition of $U = 0$ at $x = 0$ [42]. For $x = d$ and $\phi(x = d) = V_0$, limiting current for relativistic case given in Equation 2.29 can be found from the Equation 2.28.

$$J = \frac{2\epsilon_0 m_0 c^3}{ed^2} \left(\sqrt{1 + \frac{V_0}{511 \times 10^3}} - 0.8471 \right)^2 \quad (2.29)$$

2.2.3 Virtual Cathode Formation and Radiation Mechanism

When electrons enter the cylindrical drift tube region in Figure 2.2a, space-charge creates a radial electric field between the beam and drift tube [9]. Due to this electric field, potential difference occurs between beam and the drift tube wall. This potential difference (named as potential barrier in [39]) limits the transmission of the electron beam [39]. If the beam current is greater than the

limiting current, potential energy exceeds the kinetic energy of the beam. Potential well is formed and this well is large enough to stop the electron beam transport. However, since the position of the potential well fluctuates in time and space, electron beam does not stop by potential well. Partial beam transport through the drift tube and partial reflection of the beam from potential well occurs. This potential well is called as virtual cathode [39]. After the formation of VC, reflexing electrons move back and forth between the cathode and virtual cathode and this reflexing motion is one of the radiation mechanisms in vircator [43, 44]. This motion can be best seen in phase space plot that shows the momentum variation of particles along the axial direction. Diamond shape shown in the Figure 2.5 is the indicator of the formation of the VC and reflecting electrons. Radiation frequency caused by the oscillation of reflexing electrons

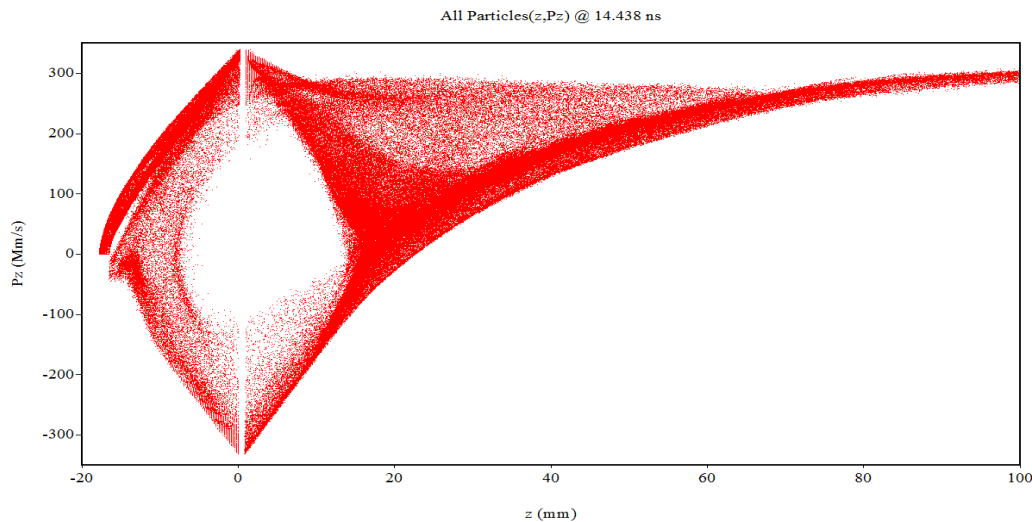


Figure 2.5: Phase Space Plot of Axial Vircator

depends on the oscillation period as follows [9, 43, 45]:

$$f_r = \frac{1}{4T} = \frac{1}{4 \int_0^d \frac{dz}{v_z}} \quad (2.30)$$

Another radiation mechanism is the oscillation of the VC itself in time and space [43, 46]. VC oscillation frequency is in the range of from w_p/π to $5w_p/4\pi$ [43, 45] where w_p is electron beam plasma frequency given in Equation 2.31. The coefficient of $5/4\pi$ was found empirically [47].

$$w_b = \sqrt{\frac{n_b e^2}{\epsilon_0 m_e}} \quad (2.31)$$

These two different oscillation mechanism was demonstrated numerically [43] and experimentally [48]. In Ref. [49], it is stated that oscillation frequency of VC increases monotonically with injected current into the drift region. Besides, when the oscillation frequency of the two microwave radiation mechanisms gets closer to each other, efficiency of vircator is reported to be increased to the range of 5 to 10% [50].

Another type of virtual cathode device designed by considering the radiation mechanisms described above is reditron shown in Figure 2.2c. Reditron was developed for the aim of eliminating the electron reflexing between cathode and VC. To accomplish this, thin annular beam was confined with axial magnetic field and thick anode structure was used with annular slit through which beam can pass. Reflexing electrons from VC are expanded radially due to transverse momentum caused by self fields and microwave generation [51]. By this way, reflexing electrons are captured by anode and radiation comes from reflexing motion is eliminated. Single mode monochromatic microwave generation was shown numerically with the reditron virtual cathode device concept [51] and the concept was demonstrated experimentally [52].

2.2.4 Double Gap Vircator

Double gap vircator in Figure 2.2e with internal feedback mechanism, enables electron beam modulation during the operation. Feedback path of the microwave is from output waveguide to modulating cavity and by this feedback, narrow band spectrum can be obtained [30]. Stability of the device is another benefit comes from the premodulation of the beam. Frequency of oscillation is strongly related with cavity dimensions of the device. It is stated that length of the cavity is arranged to $6\lambda_g/4$ [28] which gives the resonance condition for the frequency of operation. It is also given in another paper that distance between beam axis and plungers are optimized as $3\lambda_g/4$ which satisfies the condition of maximum field strengths in the beam center. In addition to this, it is reported that half power bandwidth of 15% tunability is achieved experimentally by simultaneous varying of both plungers [29]. In these studies, highly transparent anodes es-

pecially above 0.9 is employed [28, 29]. It is given that the mode of produced microwave from the radially extracted vircators is TE_{1n} in Ref. [39] and TE_{10} mode extraction is observed in radially extracted vircator in Ref. [53]. Since the extraction in double gap vircator is similar to radially extracted vircator, it is expected to obtain TE mode. TE_{10} mode extraction for double gap vircator is also reported in literature [28, 54]. Critical current calculations for this structure is given in [32, 55]. When beam current is above the first critical current, VC might be formed. Also, when beam current is above the second critical current, VC formation is the only solutions and further transmission of current is not possible [55, 56].

2.2.4.1 Literature Research of Double Anode Vircators

Double gap vircator structure, sometimes called as double anode vircator, is used without feedback window to satisfy resonant condition of the two microwave radiation mechanisms of the vircator explained in the Section 2.2.3 [50]. Resonant condition means that frequency of the virtual cathode oscillation and electron reflexing frequency is equal to each other. It is shown in [50] that microwave production efficiency is in the range of 5 to 10% when the resonance condition is satisfied. Frequency of the virtual cathode oscillation depends on beam plasma frequency in Equation 2.31 i.e. electron beam density [9]. Frequency of the reflexing electron motion is given in the Equation 2.30 and it depends on the distance. In the design, f_r is arranged by the effect of AA gap distance on the electron transit time in order to reach resonance condition.

Feedback between the output waveguide and AA gap is examined numerically in 1997 [54]. Geometry of this design is very similar to the Figure 2.2e except for the large plunger. It is stated that height of the modulating cavity is determined to make VC position in the output waveguide region. TE_{10} mode microwave extraction is observed. Two conditions for the beam diameter is proposed. In one of them, the diameter is notably less than half of the guided wavelength to achieve efficient energy exchange. The second one is that the diameter is less than size of the larger waveguide wall in order to reduce the influence on the VC

formation. Distance between small plunger and the beam center is optimized and found as $3\lambda_g/4$ in terms of guided wavelength of the waveguide. Another comment on the electron absorption of the foil is the monotonically decrease in the generation power with the increase of the absorption. Larger waveguide wall is used for frequency tuning instead of the simultaneous optimization of the coupling window size and plunger position. It is reported that 20% frequency tuning capability is achieved for this structure.

In Ref. [57], axial vircator configuration with double anode structure is analyzed under the external SHF signal applied to AA Gap. It is stated that application of this external signal make the spectrum narrower and it is observed that output power is increased with the higher amplitudes of the external signal. Another point needs to be mentioned that standing wave maximum point is placed at the beam center by positioning the piston.

Russian scientists presents an experimental demonstration of their previous work [54] by using SINUS-7 electron accelerator [58]. 1GW microwave pulses around 20-30ns in L and S band with a corresponding 5-6% efficiency result is indicated. Besides, 7% percent frequency tuning is reached when half of the maximum obtained power is considered and 20% percent frequency tuning is achieved when lower power efficiency values are considered. In addition, as an important restriction, destruction in anode meshes is shown in repetitive operation. Another experimental study with the same vircator geometry is performed with compact generator with inductive energy storage [28]. Optimum lengths of the height of the modulating cavity and output waveguide are given in terms of radiation wavelength. Plunger positions from beam center are arranged to $3\lambda_g/4$ which makes the dominant mode of cavity TE_{103} . Tungsten grid with geometrical opening of 0.95 is employed. It is indicated that radiation frequency remains the same although there are impedance variations at the input. Percentage frequency tuning in terms of the half of the maximum radiated power is given as 20%. It is pointed that advantages of this structure are mechanical adjustability of frequency, stability of radiation frequency, single mode in the radiation spectrum and no need for external magnetic field supply.

Mechanism of the microwave generation of VC containing devices are discussed [6, 29] and vircator studies with the double gap with electrodynamic feedback structure is given. Theoretical efficiency limit for two gap electrodynamic system is introduced as 20% and it is indicated that this is three times higher than one-gap with similar conditions. However, this limit is not reached in the experiment due to difficulty of simultaneous arrangement of the gap width, rf field phasing and the ratio of the RF fields in the gap stages. In the experiment, tungsten grid of mesh size $0.5\text{mm}\times 0.5\text{mm}$ with 0.9 geometrical transparency is used. It is graphically demonstrated that thinner foil leads to higher microwave radiation. Results of [54] is verified and frequency tuning is extended to 15 % by simultaneous varying of the two plungers.

Previous study of double gap vircator with inductive energy storage source [28] is further developed aiming to obtain higher microwave power [59] with a different operating frequency of 2.1GHz. Guided wavelength and longer dimension of the rectangular cross section are found as 204mm and 100mm from the given information in the paper. Distance of plungers from beam center is arranged to $3\lambda_g/4$ which gives rise to TE_{103} mode in cavity. For maximum diode voltage of 1MV, diode current of 20kA and pulse energy of 55J and pulse width of 150ns; 50 ns half power microwave pulsewidth with 1GW peak microwave power is obtained with corresponding 5% efficiency. In the experimental work, gradual decay is observed in the generated microwave and possible reasons of this pulse length limitation is investigated in simulation. Possible cause for this limitation is found as the explosive emission coming from the guard electrode of the cathode. Another suggestion for microwave decay is given as ion emission from the collector plasma. It is shown in the simulation that combined electron and ion bilateral emission in the modulating gap is the result of the dramatic drop of the output microwave by breaking the feedback mechanism. Physical explaining for this breakage is the formation of the quasi-neutral synthetic collisionless plasma which is an effective microwave absorber.

Another experiment is conducted for the same vircator structure by using a voltage source STEND Marx generator which has (700kV-800kV) peak voltage with duration 150ns and 10GW beam injection [60]. Microwave pulse duration

and energy is improved to about 70ns and 70J compared to current source in [28] due to improved stability of the electrom beam power [60]. However, it is noted that time decay of the microwave power is still observed. It is indicated that microwave pulse width is further increased by smoothing the partition wall of the structure to about 100ns and 1GW microwave peak power with 10% efficiency is obtained.

Double and single grid vircator structure are compared under relative low voltage and repetitive operation and double gap vircator is given almost three fold higher power and two fold higher energy results. Besides it is stated that double gap one has less sensitivity to the alignment precision of the gap distances [61].

In National University of Defense Technology, double gap vircator is examined both experimentally and numerically [62]. This study is the base study of the main geometry given in Figure 4.1 at the same time. Both simulation and experimental output frequency of generated microwave are found as 2.66GHz. Output power and efficiency are found 1.15GW and 11.5% numerically, 220MW and 1.15% experimentally. As an important conclusion, coupling window size and output power relation are presented and it is shown in simulation that output power graph is periodically changed for a shift of the coupling window by an amount of $\lambda_g/2$. Similar characteristic is also obtained from experimental results.

Due to gradual microwave decay observed in [59], cathode material evaluation is conducted [63]. Velvet, metal dielectric and carbon fiber cathodes are examined experimentally. Another limitation than pulse shortening over the microwave pulse length is showed as the larger AK gap distance which results in the delay in the beginning of the microwave pulse. This delay is found more than in velvet cathode while it results in longer microwave pulses of about 400ns.

Plasma formation in the double gap vircator structure is experimentally investigated with a modified cathode design over Ref. [63] which result in reduced current loss caused by radial divergence of the beam, also known as edge effect [64]. Modified cathode is tested with planar diode configuration and verifies that transmitted current ratio becomes closer to transparency [64, 56] which

limits the radial emission. Besides, peak microwave power is enhanced about 2-2.5 times with modified cathode. Calculations of energy deposited to foil show that sufficient amount of energy is deposited to anode. Light emission from the second cavity is the another indicator of the existence of plasma in the gap. Ion emission from the plasma is verified by the comparison of the calculated transmitted current and measured transmitted current. Starting of the ion emission is seen to be just after the maximum point of the microwave generation and after that point microwave generation is decayed. Due to this information, it is indicated that ion emission is the reason of the microwave decay due to VC destruction [64].

Double gap structure is adapted to the coaxial vircator [65]. Experiments are conducted by using compact linear transformer driver (LTD) whose characteristics are 300kV, 20kA and 200ns. Under this condition, 300MW peak output power and 130ns microwave pulse duration are observed. 2.2GHz operating frequency are measured and frequency tunability at half power level is obtained as 7%.

Double gap vircator experiment is conducted with collaboration of the Swedish Defense Research Agency (FOI) and French-German Research Institute of Saint-Louis (ISL). Graphite cathode is preferred instead of velvet due to electrical breakdown problems and first anode made of copper is replaced with stainless steel. Two parameters, AK distance and input voltage, is varied and at most 2kV/m peak electric fields are obtained. In addition, it is stated that generated microwave at the output tube is feed back to the modulating cavity to premodulate the electron beam [30].

A follow-up study of Ref. [63] and [64] is focused on the generation delay of microwave [56]. Since plasma is the source of the ion emission which destruct the VC, it ceases the microwave emission. It is pointed that reducing the deposited energy by reducing the current could be lengthen the microwave pulse. Reduction in current can be accomplished by expanding the AK gap. Larger AK gap leads to microwave generation delay which is the another limitation on the microwave pulse length. There is pulse shortening in the opposite end of

microwave pulse. In Ref. [56], one end of the shortening, generation delay, is examined. It is shown that generation of microwave is delayed for larger AK gaps for a fixed accelerating voltage or lower accelerating voltages for a fixed AK gap. Experimental confirmation of the beam pinching is done. Minimal current required for the VC formation and microwave generation is considered to lower energy deposition to foil. Starting current values of the 22 shots are determined and compared with the theoretical critical current values given in Ref. [55]. According to comparison, larger input current value from the second critical current is determined as the condition not only for VC formation but also sufficient percentage for the reflected electrons. Maximum FWHM output pulse duration is achieved as 180ns. In addition, the interval of the beam current which leads VC formation without microwave generation because of insufficient amount of reflected currents is shown. Also, this is confirmed with numerical simulations.

Double gap structure is proposed as microwave amplifier by using VC formation [66]. In this structure, feedback between the output cavity and modulating cavity is closed and signal is injected to the modulating cavity. TM_{110} mode is excited by coaxial waveguide in CST Particle Studio simulation environment. It is shown that, virtual cathode amplifier(VCA) does not provide output in the absence of the input RF signal. In the presence of the RF signal excitement, gain of 4.7 is obtained in terms of signal amplitude. The structure is tested numerically for varying signal amplitudes at fixed frequency and for varying frequencies at fixed signal amplitude. First, optimum signal amplitude is found in which power gain is 65. It is noted and shown that, output signal is significantly reduced for lower amplitude signal levels due to insufficient modulation and for higher amplitude levels, reduction on the output signal level is observed due to overmodulation. Frequency tuning is achieved by using tuning plunger which effectively change the length of the modulating cavity. After 1.15GHz, drop on power gain is observed due to reduction in the interaction efficiency.

To conclude, double-gap vircator draws attention in literature due to stability and tunability of frequency of generation and efficient microwave radiation result from electron beam premodulation. Experimental results of 15% half power

bandwidth tunability and 10% power efficiency in terms of peak power of 1GW with a pulse duration of 100ns can be seen as noticeable results of this type of vircator [29, 60]. Need of higher transparency of anodes could be practical problem in laboratory conditions.

2.2.5 Effect of External Signal

External field injection to vircator is used for various purposes with desired improvements on the system although it is stated that no observable effect is indicated on the vircator when X band signal is injected by magnetron [53]. Frequency control of vircator is achieved with external signal whose frequency is close to one produced by device [67]. Amplification usage of the vircator is demonstrated under externally applied input RF signal experimentally [68, 69]. In addition to this, it is shown numerically that double gap vircator can be used as amplifier when signal is injected to the modulating cavity region [66]. Another purpose of external harmonic signal usage is to enhance output power extraction. Numerical and experimental studies indicates that external single frequency signal affects low voltage vircator by giving velocity modulation to the beam and it increases the output power of device. Also, it is indicated that highest power is observed when the applied signal frequency is close to natural VC oscillation frequency [70, 71]. Another application area is phase locking aiming to drive vircator with other master oscillator such as magnetron [10, 11, 12, 13].

2.2.6 Axial Vircator with Feedback Structures

Axial vircator shown in Figure 2.2a has very simple geometry compared to other types given in Figure 2.2. Space charge limiting current for the axial vircator with cylindrical drift tube is given in Equation 2.32a for annular beam and in

Equation 2.32b for solid beam [9].

$$I_{SCL}(kA) = \frac{8.5}{\ln(r_0/r_b)}(\gamma_0^{2/3} - 1)^{3/2} \quad (2.32a)$$

$$I_{SCL}(kA) = \frac{8.5}{1 + \ln(r_0/r_b)}(\gamma_0^{2/3} - 1)^{3/2} \quad (2.32b)$$

where r_0, r_b, γ_0 are radius of tube, radius of beam and relativistic factor for incoming beam respectively. Formulation for the frequency prediction in axial structures is given in Equation 2.33 [5, 72].

$$f(GHz) = \frac{4.77}{d(cm)} \ln[\gamma_0 + (\gamma_0^2 - 1)^{1/2}] \quad (2.33)$$

where d is AK gap distance in cm. When the beam enters to cylindrical geometry, only nonzero fields are E_z, E_r and B_θ which allows TM mode propagation [39, 49]. Moreover, space charge cloud couples with radial and axial components of electric field which likely give rise to TM_{0n} modes [1].

The main aim of usage of feedback structures in vircator is to strengthen interaction between beam and field at VC area and force the oscillations to frequency of cavity [1]. Higher output power values are obtained for various feedback components as a result of stronger beam field interaction [1, 73, 74]. Another advantage of usage of feedback is to reduce reverse energy transfer from EM fields to electrons along output drift tube or using the escaping electrons in MW generation [1, 31]. Bar reflector in coaxial vircator has noticeable results with enhancement of power by a factor 1.5 [74] however in this part of thesis, axial geometries are the region of interest. Annuluses and reflectors are examined and literature survey is given in the following two sections.

2.2.6.1 Feedback Annuluses

Feedback annulus in axial vircator configuration is presented by aiming to feed back the VC area [75]. Considered annulus shape is ring with outer radius is exactly equal to enclosing drift tube. In the study, open resonator is formed with annulus and frequency of output spectrum is obtained in compatible with resonator modes. Less than 10% bandwidth is obtained numerically. Experimental confirmation is given also however frequency difference between numerical and

experimental results is left unexplained. Above 300MW power is stated to be obtained with approximately 3% efficiency which is found from given rough input voltage and input current values. In a follow up study, device is compared with no annulus case and average output power is shown to increase from 94MW to 335MW [73]. Aperture radius is optimized and advantage of thinner annulus is shown also in the same paper.

Novel configuration of three cavity vircator shown in Figure 2.2f is examined in both numerically and experimentally [19]. According to the paper; first cavity forms between foil and first annulus enhances power conversion efficiency, second one improves the extraction efficiency of microwave power and the last one reduces reflection of electromagnetic wave from the output. However reasonings of these cavity effects does not mention in the paper. In addition, more than two fold improvement of microwave conversion efficiency over one annulus structure is given for simulation results. 6.6% efficiency is obtained with radiation frequency consisted with numerical outputs.

For the resonant frequency calculations of the cavities resulted from feedback annuluses, equivalent circuit method is proposed and verified with simulation results [76]. In addition, frequency stability of device in each range of (588kV-717kV) AK gap voltage and (12mm, 16mm) AK gap distance is demonstrated.

As a different approach, three cavity structure is considered as microwave filter and S parameters are found to show the bandpass filter characteristic for annuluses [31]. Besides, absorbing of down-streaming electrons by annuluses is shown with phase spaces and this effect is considered to increase output power by reducing energy of accelerated electrons beyond last annulus. Aim is indicated as optimizing the device with lower AK gap voltage values.

Three cavity resonators designed in [31] is simulated and optimal radius of electron beam is found [77]. Experiments of the simulations in Ref. [31, 77] is conducted with ring type and solid cathodes with different radii [78]. Although frequency matching with simulation is achieved for some of the cathode trials, output power is below the value predicted in simulation. Observed lack of repeatability of the device is associated with homogeneity and energy spread of

the electron beam.

2.2.6.2 Reflectors

Reflectors with unity electron transparency is introduced to axial vircator in the aim of enhancing power conversion efficiency as indicated in shown in Figure 2.6 [1]. Geometry of used reflectors is selected solid disk with an annular opening between drift tube wall and them in order to allow MW propagation to output of the device. In addition, quasi cavities is formed between two consecutive anode or reflectors. Reflectors, also can be called as anodic foils, has two important role in the device. First one is to form more than one VC along drift tube. By this way, waste energy by electron flow is used for microwave generation. Second one is to form quasi cavities wherein EM fields occurs which leads to stronger beam field interaction. Radial electric field distribution of the TM_{01} fields is played important role in the selection of radii of the reflectors. Radius of each reflector is chosen to cover the maximum field point of radial electric field distribution in order to efficient trapping of EM fields. Selection of longitudinal positions of reflectors is arranged according to make the position of first VC at the center of distance between anode and first reflector. Each reflector is positioned as equidistant to consecutive ones. Frequency of operation is stated as $3.18GHz$ for no reflector case and gradual decay till 2 reflector case. For adding of more reflectors, frequency is said to be preserved in the range of $2.86 - 2.88GHz$. According to the dimensions given in Ref. [1], resonance frequency of quasi cavity is calculated as $2.92GHz$ which is pretty close to given TM_{01} radiation frequency. Optimum efficiency value is obtained with three reflectors case and in this case it is given that $1.26GW$ average MW power at $2.88GHz$ with nearly 13% power conversion efficiency is obtained numerically which is roughly 12.8 times higher power than the one in standard configuration. Reason of efficiency drop for more than 3 reflectors is shown as the mode competition between TM_{01} and TE_{11} . Later, mode competition problem is solved by decreasing radii of reflectors after third one [18]. With an optimal configuration of 5 reflectors, it is expressed that about $2GW$ average output power with corresponding 21% power conversion efficiency at $2.86GHz$ is numerically reached.

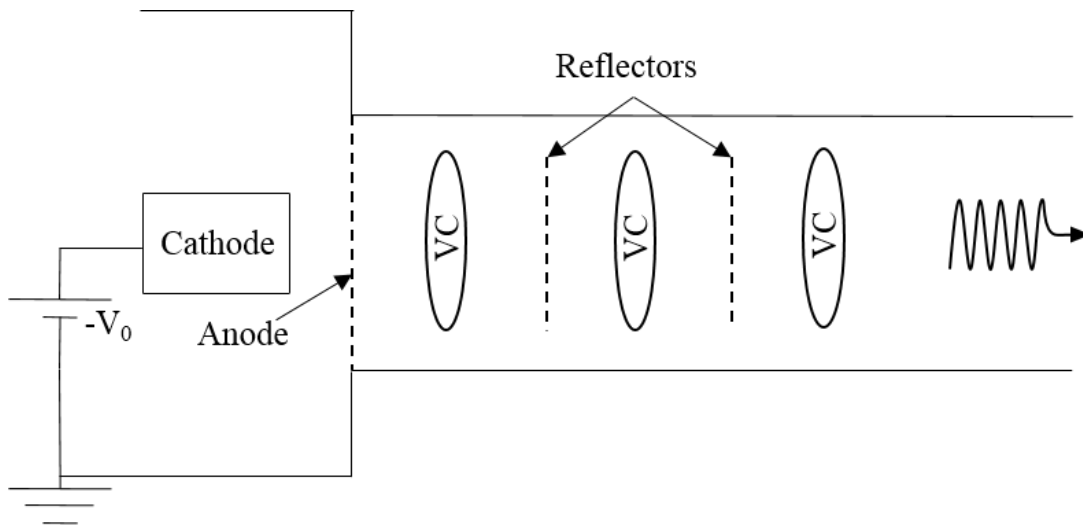


Figure 2.6: Axial vircator with reflectors presented in Ref. [1]

CHAPTER 3

VIRCATOR SIMULATION ENVIRONMENT : MAGIC TOOL SUITE

Magic Tool Suite is the electromagnetic (EM) Finite Difference Time Domain (FDTD) Particle in Cell (PIC) simulation software that is used to solve interactions between EM fields and particles. It has broad application area in the plasma physics problems. Users configure the software by defining geometry, material types and entering field and particle algorithms. Since, number of particle in a problem generally excess the memory of computer, macro particles are defined in simulation. Macro particles have same particle to mass ratio with the particle in the physical problem [2]. Magic uses Maxwell's Equation in Equation Set 3.1 and constitutive relations in Equation Set 3.2 to obtain EM fields and uses Equation Set 3.3 to get particle trajectories with found EM fields. With continuity equation in Equation 3.4, required charge and current densities for Maxwell's Equations are found [3]. These steps define loop process which is indicated in the Figure 3.1.

$$\frac{\partial \bar{B}}{\partial t} = -\nabla \times \bar{E} \quad (3.1a)$$

$$\frac{\partial \bar{D}}{\partial t} = \nabla \times \bar{H} - \bar{J} \quad (3.1b)$$

$$\nabla \cdot \bar{D} = \rho \quad (3.1c)$$

$$\nabla \cdot \bar{B} = 0 \quad (3.1d)$$

$$\bar{D} = \epsilon \bar{E} \quad (3.2a)$$

$$\bar{B} = \mu \bar{H} \quad (3.2b)$$

In these equations; \bar{D} and \bar{B} are electric and magnetic flux density, \bar{E} and \bar{H} are electric and magnetic field intensity, \bar{J} and ρ are current and charge densities, ϵ and μ are the permittivity and permeability respectively.

$$\frac{\partial p_i}{\partial t} = \frac{F_i}{m_i} = \frac{q_i}{m_i} (E(x_i) + v_i \times B(x_i)) \quad (3.3a)$$

$$\gamma_i = (1 + |p_i/c|^2)^{1/2} \quad (3.3b)$$

$$v_i = p_i/\gamma_i \quad (3.3c)$$

$$\frac{\partial x_i}{\partial t} = v_i \quad (3.3d)$$

where; p_i , v_i , γ_i , m_i and q_i are momentum, velocity, relativistic factor, mass and charge of the i^{th} particle.

$$\nabla \cdot \bar{J} = -\frac{\partial \rho}{\partial t} \quad (3.4)$$

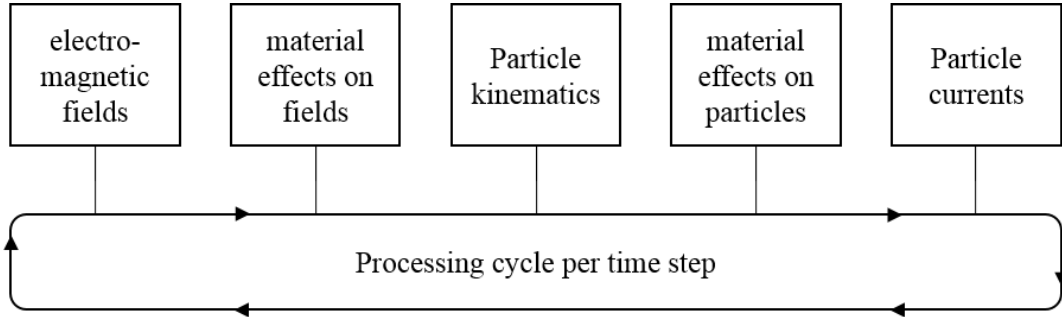


Figure 3.1: The processing cycle [2]

In process shown in Figure 3.1, discretization in time is applied according to Figure 3.2. Electric fields are calculated at the integer time steps while magnetic fields are calculated at the integer plus half time steps. This process is called as leapfrog algorithm. Discretization in space is applied to the problem according Yee cell given in Figure 3.3a. Spatial coordinates are divided into small boxes called grid, electric and magnetic fields are located to the corners and face centers of the full and half grid cells given in Figure 3.3b.

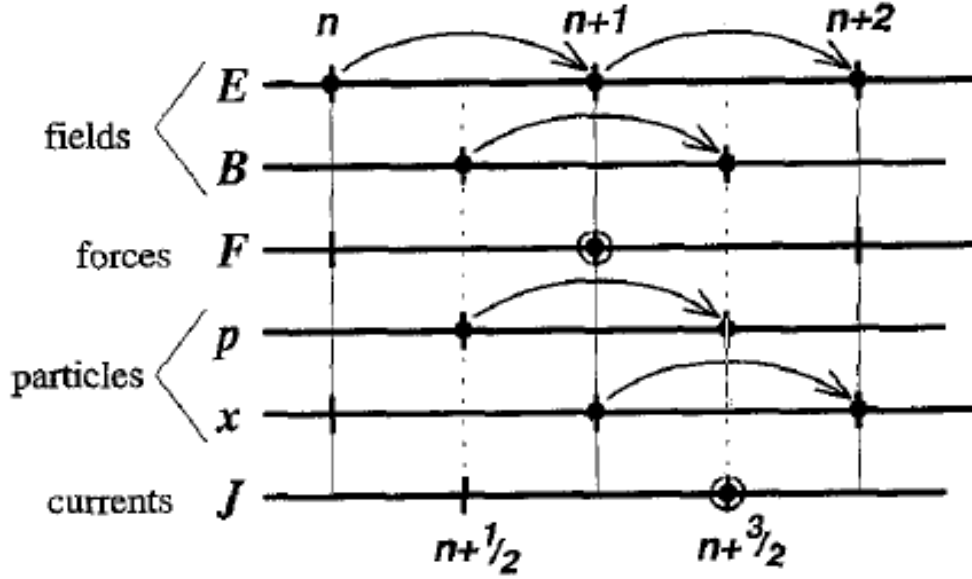


Figure 3.2: Leapfrog time integration scheme [2]

For the selection of the grid dimensions, ten grids per wavelength is used as rule of thumb. Another criteria for the grid dimension is the placing at least ten grid cells between the anode and cathode region in which most intense interactions between electron beams and EM fields take place. This criteria is based on the conversation with Magic Help Desk.

Important stability criteria in Magic simulations is defined with Courant Stability given in Equation 3.5:

$$c\Delta t \leq \sqrt{\frac{1}{\frac{1}{dx^2} + \frac{1}{dy^2} + \frac{1}{dz^2}}} \quad (3.5)$$

where c is speed of light; dx , dy and dz are grid dimensions along x , y and z and Δt is simulation time step. This criteria implies that EM wave should not propagate more than one cell in a EM time step. Magic takes the electromagnetic time step as default value of 0.85 of the courant time step comes from Equation 3.5 [3]. EM time step, Δt , of the simulation can be specified externally by using TIME_STEP command [3].

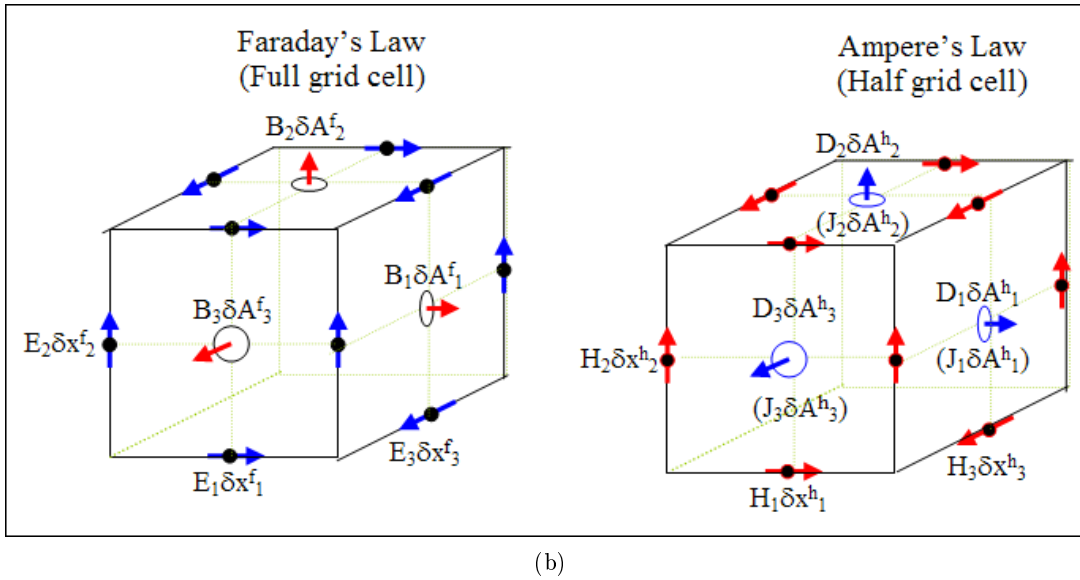
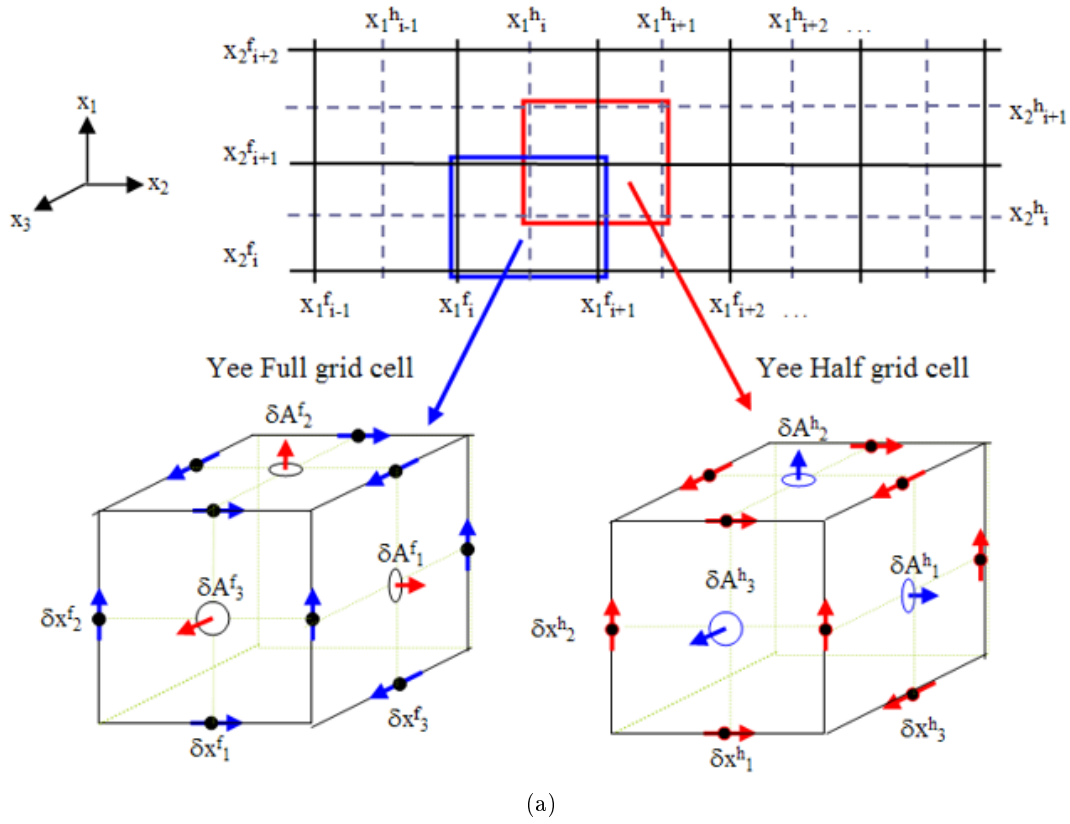


Figure 3.3: (a) Yee cell [3] (b) Location of electric and magnetic fields in half and full grid cells [3]

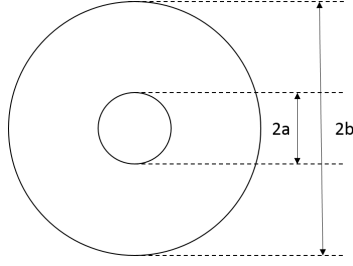


Figure 3.4: Coaxial shape of input

3.1 Applying of Pulse Voltage Waveform

Voltage pulse signals are applied to vircator in Magic by using PORT command [3]. Magic injects EM wave from the input port therefore time and spatial variation of the desired EM wave should be specified in PORT command. Multiplication of the temporal function and spatial profile function gives the desired input signal. Spatial profile function can be entered by using 3 option: Function, File, Laplacian. Function option requires transverse spatial distribution functions in preselected coordinate system. File option is used to read the record of the previously simulated geometry from a file. Laplacian option computes the laplacian equation in the port boundary and solves the spatial distribution numerically. For an axial vircator configuration given in Figure 2.2a, input port has coaxial shape as in Figure 3.4 and electric field variation on this shape is given in the Equation 3.6 when potentials of the inner and outer conductors are taken as $-V_0$ and 0 respectively.

Laplacian and function options are used separately and voltage signal at the input are compared in Figure 3.5 which shows the plots on the top of each other for two option. Mean values of the voltage waveforms between $10ns$ and $40ns$ are computed as $87.14kV$ and $87.16kV$ for function and laplacian options respectively. In addition to this, polarity of the normalization line is important to correctly applying the waveform at input. Wrong application results in no emission from the cathode surface.

$$\vec{E} = \frac{-V_0}{\ln(b/a)} \frac{1}{r} \hat{a}_r \quad (3.6)$$

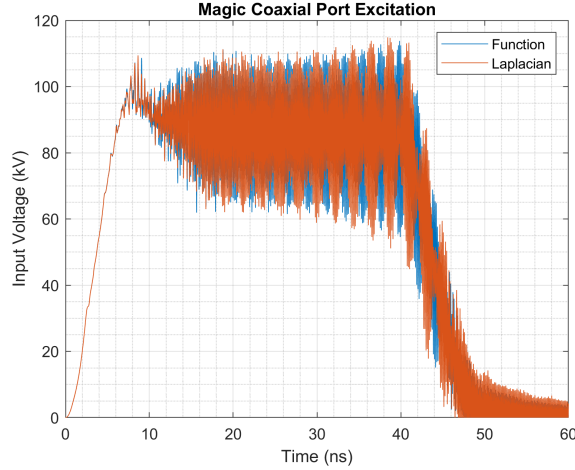


Figure 3.5: Input signal of the axial vircator for different excitation

3.1.1 Usage of Circuit Option in Port Command

Temporal function used in the PORT command specifies time dependency of incoming wave at the port. Measured voltage at the input terminal gives the summation of both input and reflected wave [3]. To arrange specific value for the measured voltage value at the input, also at the anode cathode gap for axial vircator case, two method can be used. Firstly, user can determine the incoming wave voltage value iteratively. Secondly, circuit option in PORT command can be used. Circuit option provides a feedback loop that rescales the incoming field to equalize the desired value. Three parameter should be given to Magic. First parameter is the time constant. Selection of the time constant is not straightforward because in the help document it says that user must choose time constant by using physical intuition, experience, common sense and trial and error [3]. Second parameter is desired voltage waveform. Third parameter is the measured waveform of the signal to which feedback loop applies. In this work, base value of the selection is chosen as the rise time of the input voltage waveform. Time constant is halven at every step and convergence to desired waveform is checked. Initial test runs are performed by using Magic example "DCPortCircuit" whose geometry shown in Figure 3.6. For a 5V peak voltage value, different rise and fall times are tested with varying time constants. One of the result is shown in Figure 3.7. In this figure, different

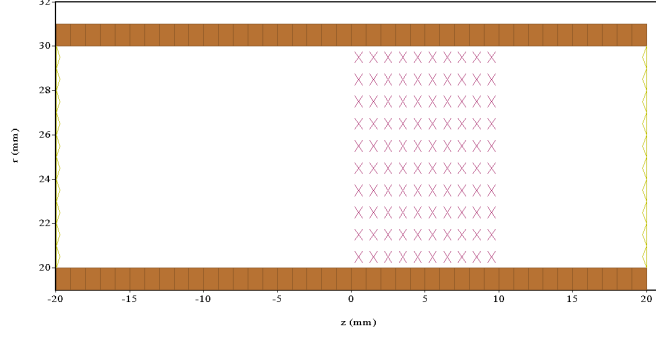


Figure 3.6: Coaxial test geometry for port circuit

Table 3.1: Mean input voltages on the flat region of waveform

Time Constant (ns)	$T_{rise}/2$	$T_{rise}/4$	$T_{rise}/8$	$T_{rise}/16$	$T_{rise}/32$	$T_{rise}/64$
Mean Voltage (kV) (20ns,25ns)	282.73	288.51	295.78	298.84	299.61	299.85

port circuit values are compared with the case of without port circuit (dark blue curve with approximately 2.5V peak voltage) and the desired waveform (black curve). Zoom-in plot in Figure 3.7 shows some overshoot might be observed for lower time constant values. Due to this overshoot $T_{rise}/16$ seems to give good results to the desired value of waveform. After this, port circuit is tested with axial vircator by adding the effect of electron emission from cathode. Result is shown in Figure 3.8. Besides, Table 3.1 shows the mean voltage values of applied waveforms in flat region. 300kV peak value is desired for the input side. According to this figure and table, $T_{rise}/16$ gives again promising results for converging to desired waveform. Therefore, $T_{rise}/16$ is chosen for this thesis work.

3.2 Anode Modeling

Anode modelling in Magic is performed by using either FOIL or FILM command. FILM command offers to choice finite conductivity and dielectric for the anode material while in FOIL command anode is assumed to have perfect conductivity [3]. In Ref. [3], it says that incoming electron beam to foil or film experiences

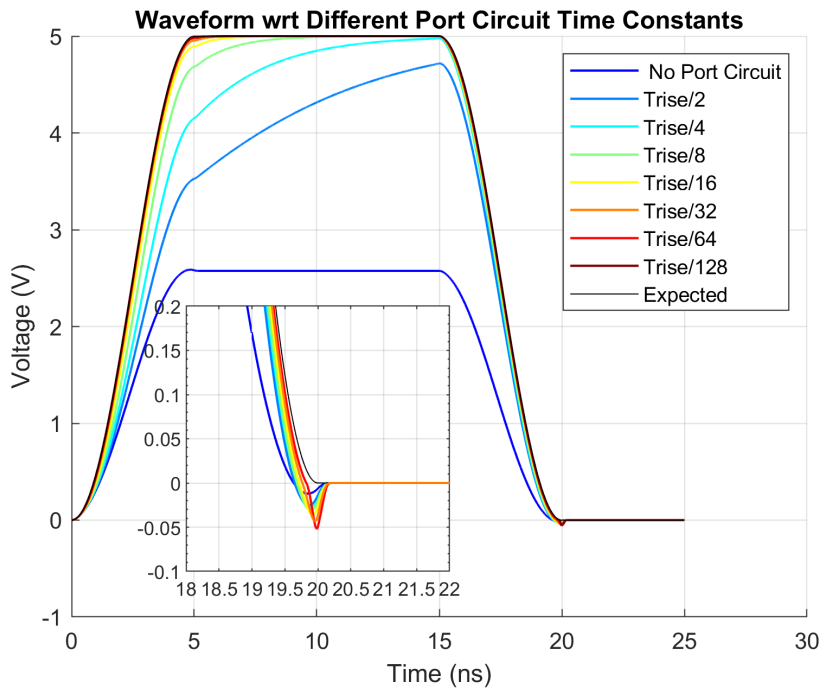


Figure 3.7: Signal excitation to coaxial structure with port circuit

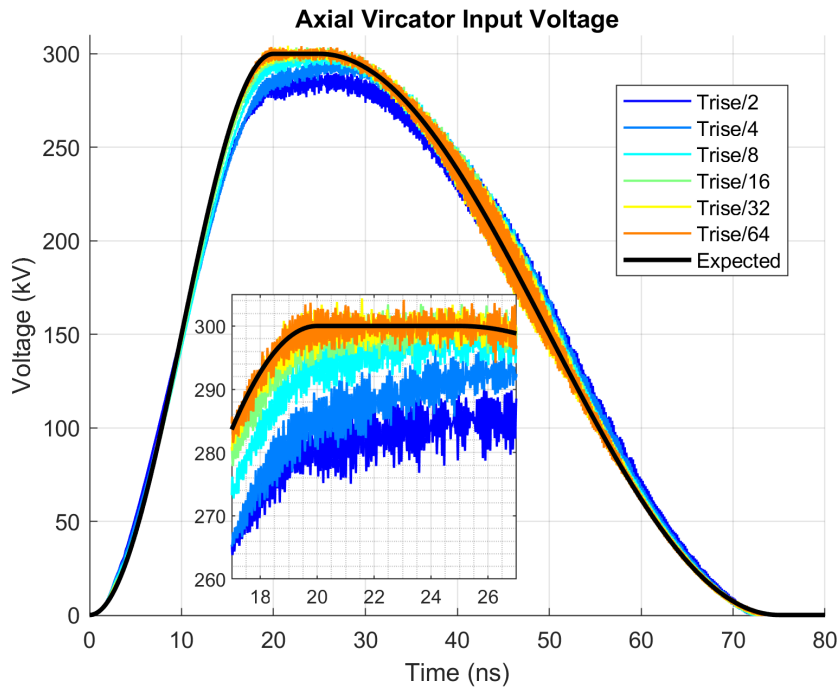


Figure 3.8: Magic input Signal of the axial vircator for different port circuit time constant

scattering, energy loss, or deposition in foil or film. This complicated process is modeled by subroutines from Integrated TIGER Series of codes (ITS 3.0) in Magic. In this thesis study, FOIL command is used for modeling anode behavior. In the FOIL command, electron transmission is determined by two model. First one is "Fraction" model that controls the ratio of the undeflected transmission electrons to incoming electrons. Second one is "Grid" model which model anode as grid structure. Both of the two models are tested by using examples of the simulation.

Besides, noticable studies were published aiming more realistic numerical analysis of foil. Energy dependent foil transparency was proposed and it was said that fairly good agreement with published experimental results is obtained [79]. Years later, foil ablation effect and gap closure due to anode plasma were also taken into account for numerical analysis [80].

3.2.1 Fraction Model

Base simulation model for this part is "3DFoil" example file of the Magic. Figures 3.9a shows the geometry of the file in the $r - z$ plane. It has cylindrical symmetry around the shown plane. Material of the foil is gold and emission process is selected as beam because of the minimizing purpose of the effect of electron beam energy spread on foil behavior. Two different electron species are defined in the simulation namely, red electrons and blue electrons. Red electrons are defined as emission species while blue electrons exit species of the foil. This process can be seen in Figure 3.9b and 3.9c. By defining different species, it is possible to measure the scattering electron on each side of the foil by blue electrons, also to measure incoming and uninterruptedly moving electrons by red electrons. For the foil test, beam energy interval is selected in between $100keV$ and $500keV$ because it corresponds the possible gap voltage interval when commercial Marx generators are examined. Foil thickness is varied from $10um$ to $100um$ because backward scattering can be observable within this interval as seen in Figure 3.10c. In addition to these two parameters, foil transmission fraction value in FOIL command is varied from 0 to 1.

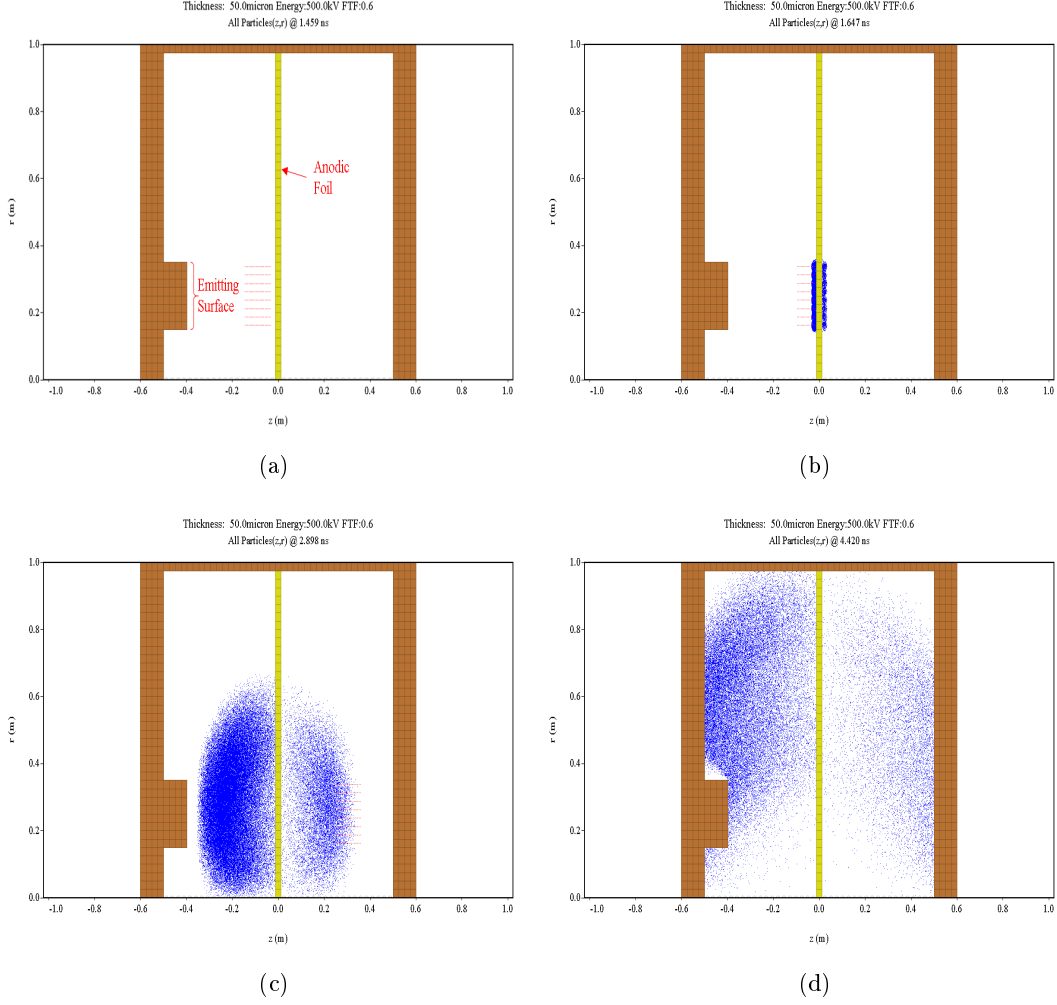


Figure 3.9: Phase space for the foil test at (a)1.459ns (b)1.647ns (c)2.898ns (d)4.42ns

For all simulation runs; undeflected transmission, forward scattering, backward scattering and capture ratios to incident electrons are calculated and plotted in the Figures 3.10. For the simulations shown in Figure 3.10, foil transmission ratio is kept as 0.6. This directly effects the undeflected electron ratio as shown in the Figure 3.10a. From Figure 3.10b, dependency of the forward scattering electrons on the foil thickness and beam energy. When more energetic electrons penetrate to foil, more forward scattering electrons are resulted in. Besides, thicker foil prevents scattering of electrons in forward direction and leads to more scattering in backward direction as seen in Figure 3.10c. From the same figure, it can be understood that backward scattering ratio for the beam is inversely proportional with the beam energy. Last type of the electrons is the captured

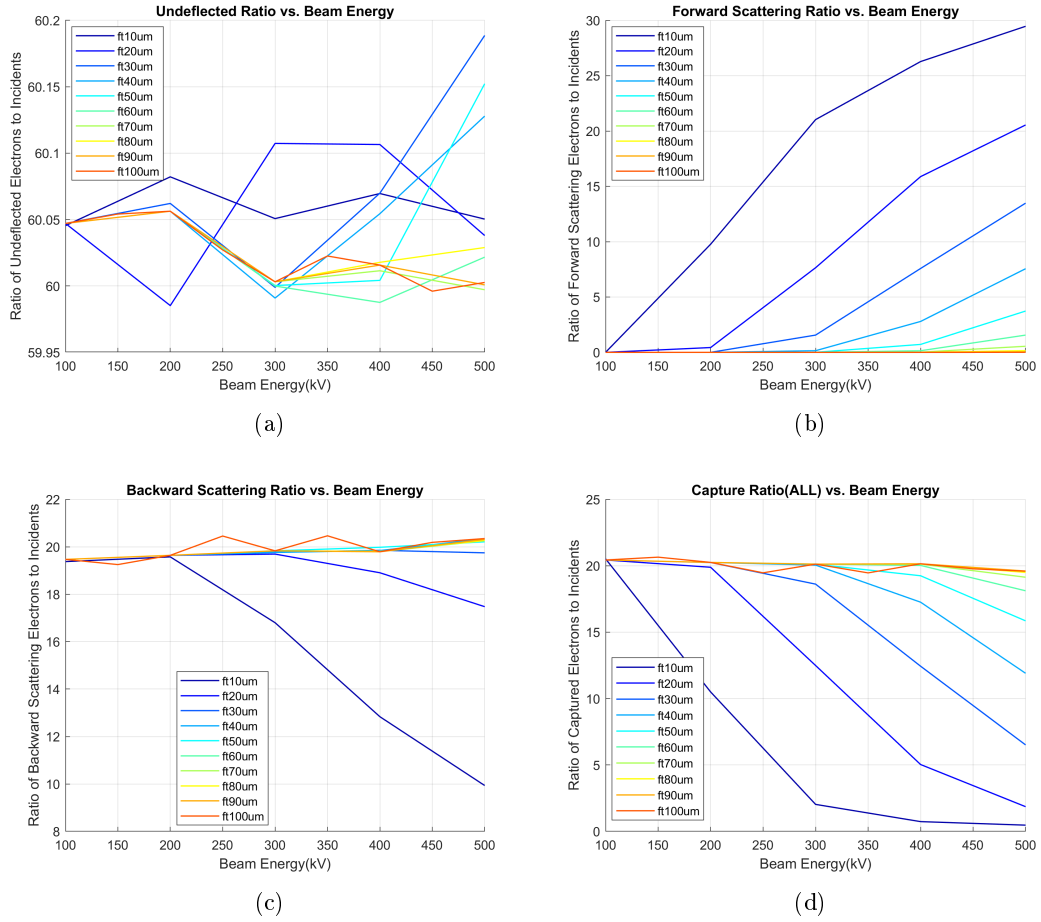


Figure 3.10: Electron ratios for 0.6 foil transmission fraction value with respect to beam energy and foil thicknesses. (a)Undelected electron ratio vs. Beam energy (b)Forward scattering electron ratio vs. Beam energy (c)Backward scattering electron ratio vs. Beam energy (d)Captured electron ratio vs. Beam energy

ones and capture ratio is increased with foil thickness and it is decreased with beam energy. Apart from the foil thickness and incident beam energy, another factor that affects foil behavior is the material type of foil. This effect will be examine in the next part together with grid foil model.

3.2.2 Grid Model

In experiments, mesh type anodes are commonly used [45, 25, 81, 82]. This can be modeled in Magic by the parameters as indicated in Figure 3.11. Start point, width and pitch values are the input parameters of the Magic model. Same

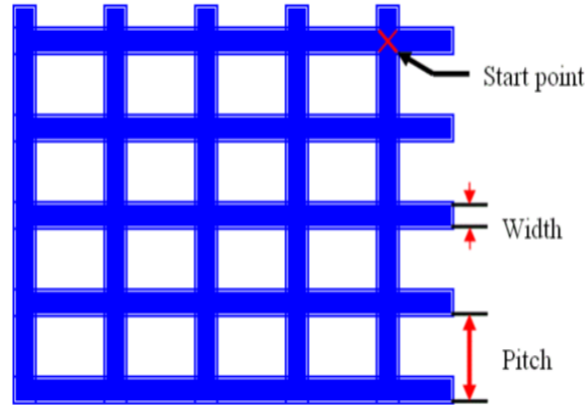


Figure 3.11: Magic foil grid model

test run is arranged to grid model and phase space of the beam cross section is checked to view the grid structure. It can be seen from Figure 3.12, grid structure is conformal to the coordinate system. Since the grid structure used in literature has cartesian symmetry, test run is rewritten based on the initial run in cartesian coordinates. Planar emission is defined instead of pencil beam in the Figure 3.9a because of holes in the grid. Pencil beam cannot pass grid if it hits grid wire. This gives the wrong calculation of the ratios given in Section 3.2.1.

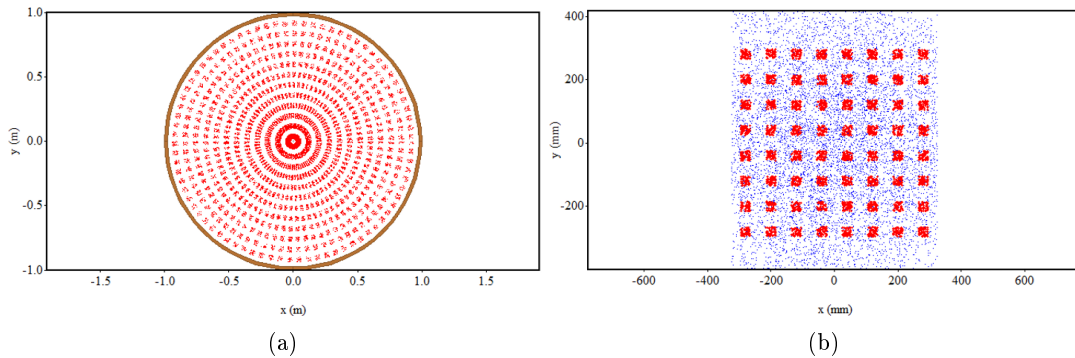


Figure 3.12: Grid models in Magic for (a)cylindrical and (b) cartesian coordinate system

Figure 3.13 shows the test simulation for cartesian coordinate system. Same as Figure 3.9, red electrons shows incoming beam and uninterruptedly moving beam electrons while blue electrons shows scattering electrons at the each side of the foil. For each simulation performed with grid foil, corresponding fraction

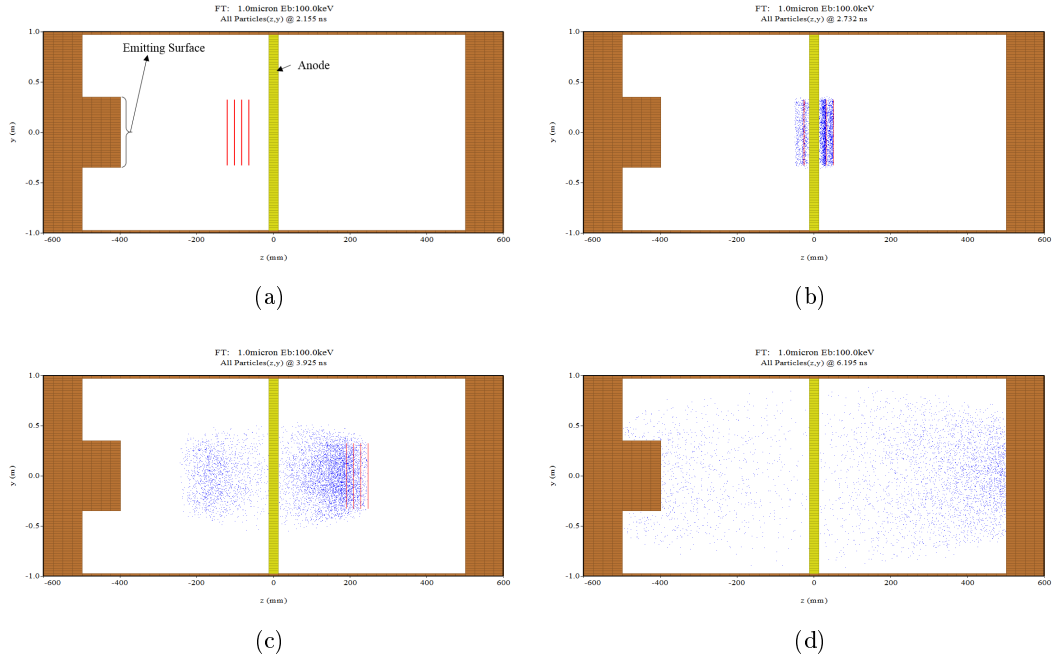


Figure 3.13: Phase space for the foil test at (a)2.155ns (b)2.732ns (c)3.925ns (d)6.195ns

model foil is analyzed at the same geometry for cross check purposes. For a foil transmission fraction, undeflected electron ratio found from grid model is entered as fraction value.

In these test runs; effects of grid dimension, width, pitch, start point, geometrical opening, material type, beam current, foil thickness and beam energy is investigated. Scattering ratio is found to be dependent on geometrical opening, material type, foil thickness and beam energy.

Table 3.2 shows the effect of material while Table 3.3 includes the effect of geometrical opening of gold grid. It is observed that more or less same results are obtained when foil transmission fraction and geometrical opening values are close to each other. Both values directly affects the undeflected electron transmission ratio and remaining electron distribution is determined by ITS 3.0 codes for both model. For this part, foil thickness value is taken as $200\mu m$. That is the reason why forward scattering ratio is found as 0. Besides, Figure 3.10a gives the tendency of forward scattering electrons to 0 as the foil is getting thicker. Dependence of foil thickness and beam energy is in consistent with the

Table3.2: Effect of material on foil behavior

	Grid	Fraction	Grid	Fraction
FTF	–	0.05104	–	0.05107
Geometrical Opening (%)	5.08	–	5.08	–
Material	Gold	Gold	Carbon	Carbon
Undelected Transmission Ratio (%)	5.104	5.192	5.107	5.041
Forward Scattering Ratio (%)	0.000	0.000	0.000	0.000
Backward Scattering Ratio (%)	46.100	45.919	3.746	3.768
Ratio of Capture Electron To Incident (%)	48.683	48.791	91.132	91.176
Sum of Ratios (%)	99.887	99.902	99.985	99.985



Figure 3.14: Magic field measurement points for mode analysis in (a)cylindrical waveguide (b)rectangular waveguide

findings in the Fraction model part.

3.3 Mode Distribution in Magic

Determining mode of the generated field in the waveguide drift tube is possible in Magic. Electric and magnetic fields in three axes are observed separately in the points seen in the Figure 3.14 and their frequency transforms are obtained. For generated microwave frequency, field strength values of each electric and magnetic field fourier transform are taken. This values are compared with the theoretical field distribution along the points in Figure 3.14. Figure 3.15 verifies the mode field distribution of cylindrical waveguide is TM_{01} . Furthermore, Fig-

Table3.3: Effect of geometrical opening on foil behavior

	Grid	Fraction	Grid	Fraction	Grid	Fraction
FTF	–	0.04919	–	0.49697	–	0.95115
Geometrical Opening (%)	5	–	50	–	95	–
Undelected Transmission Ratio (%)	4.919	5.007	49.697	49.789	95.115	95.070
Deflected Transmission Ratio (%)	0.000	0.000	0.000	0.000	0.000	0.000
Reflection Ratio(%)	-46.220	-46.144	-24.395	-24.408	-2.440	-2.467
Ratio of Capture Electron To Incident (%)	48.750	48.739	25.836	25.740	2.437	2.456
Sum of Ratios	99.888	99.890	99.927	99.936	99.991	99.992

Figure 4.4 shows the TE_{10} mode distribution of generated EM field in rectangular drift tube found by using mode analysis described here.

3.4 Data Filtering

Magic offers data filtering options in order to smooth out the measurements. Filtering can be used in the Poynting's vector measurement in the numerical analysis since it contains the twice the frequency oscillations of the wave. One of the filtering option is low pass filtering. In this filter, classical RC filter is used [3]. In a continuous time domain, relation between input and output signal for RC low pass filter is:

$$\frac{v_{in}(t) - v_{out}(t)}{R} = C \frac{dv_{out}(t)}{dt} \quad (3.7)$$

Transfer Equation 3.7 to the discrete domain.

$$\frac{v_{in}[n] - v_{out}[n]}{R} = C \frac{v_{out}[n] - v_{out}[n-1]}{\Delta t} \quad (3.8)$$

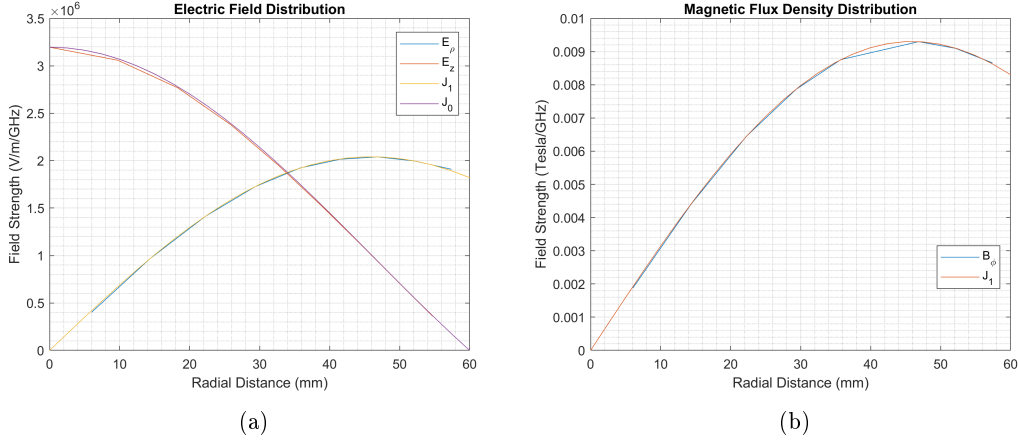


Figure 3.15: TM_{01} mode distribution of (a) electric field intensity (b) magnetic flux density

Following expression for the output signal can be obtained from Equation 3.8.

$$v_{out}[n] = v_{in}[n]f + v_{out}[n-1](1-f) \quad (3.9)$$

where f is $\frac{\Delta t}{\Delta t + RC}$. Note that Equation 3.9 is very similar for the equation given in [3]. However, filter time constant parameter in Magic corresponds to RC instead of $1/RC$ as indicated in [3].

Another type of filter is step filter which uses the following formulation [3].

$$g(t) = \frac{1}{t_{filter}} \int_{t-t_{filter}}^t s(t') dt' \quad (3.10)$$

Equation 3.10 is basically gives average Poynting's vector if $s(t')$ is the instantaneous Poynting's vector and t_{filter} is selected as the period of monochromatic wave. For the both filter, output data of Magic is processed in Matlab by using the equations described above.

CHAPTER 4

DOUBLE GAP VIRCATOR SIMULATION RESULTS

Double gap vircator examined in this thesis is given in Figure 4.1 and it is based on Ref. [62]. This structure has its internal feedback mechanism to the gap between anodic foils in order to premodulate the electron beam. As a result of this premodulation, efficiency enhancement and frequency purity is obtained. Virtual cathode forms in the output tube region and generated microwave is coupled into modulating cavity via coupling window.

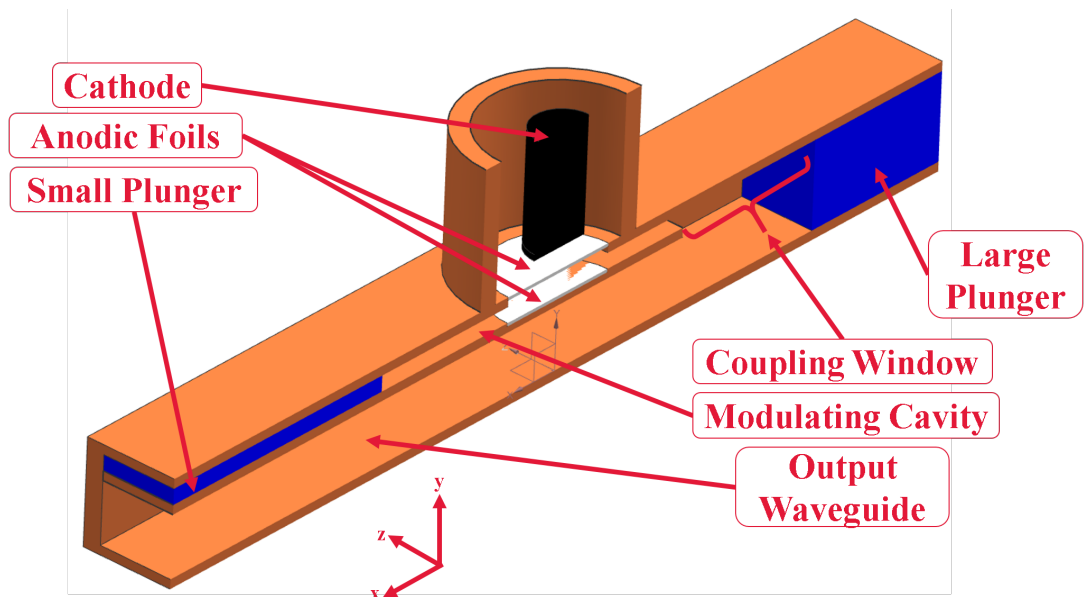


Figure 4.1: Double gap vircator

In the initial structure, VC formation is checked and location is found in beyond the second anode as expected. Figure 4.2 shows the phase space plots about VC formation. Generated EM field in the output tube, is the source of feedback

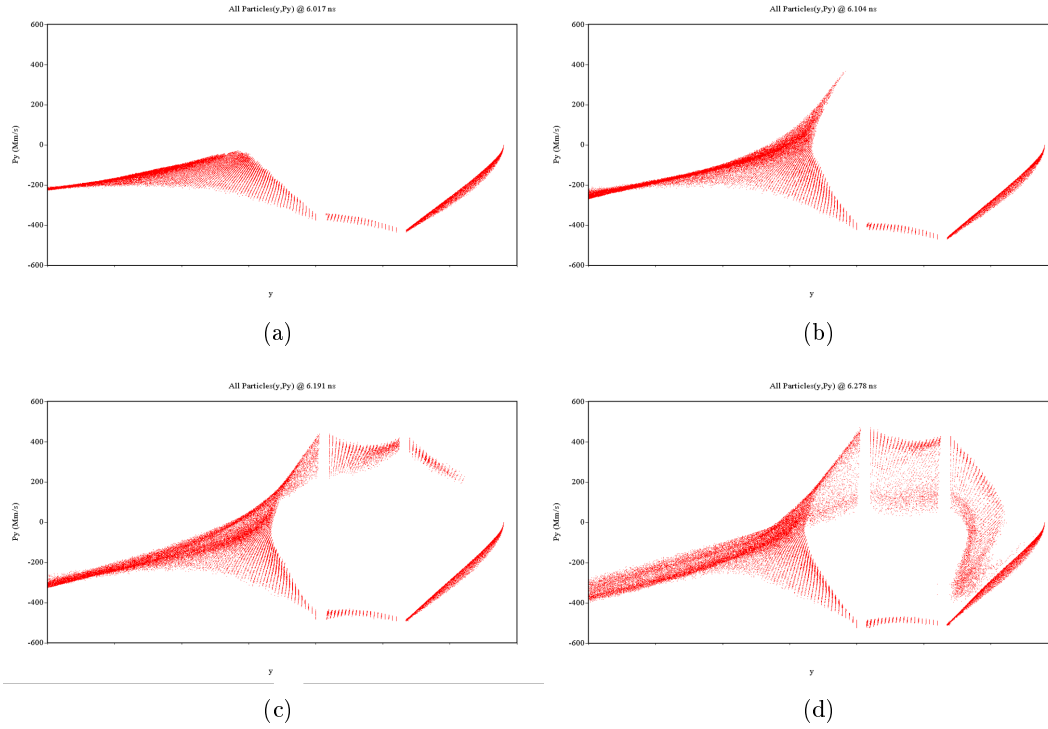


Figure 4.2: P_y vs. y phase space of double gap vircator (a)6.017ns (b)6.104ns (c)6.191ns (d)6.278ns

to modulating cavity. Frequency of operation is found by using the FFT data process of the simulation. y component of the electric field at the output is observed and its FFT result is given in Figure 4.3. From this figure, operating frequency is found as 3.02 GHz .

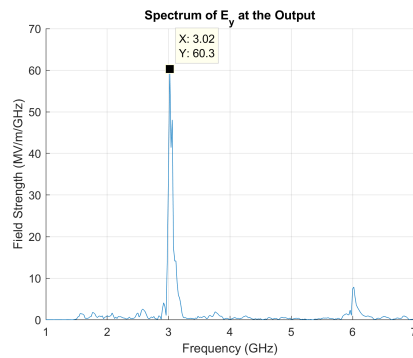


Figure 4.3: Microwave spectrum at the output of the device

Since only difference between the cross sections of modulating cavity and output waveguide is their short edge, their cutoff frequencies for TE_{01} and TE_{02} are equal to each other. For the same reason, wavenumbers and guided wavelengths

in both modulating cavity and output waveguide is identical to each other. In addition; at this frequency, mode is probably TE_{01} because cutoff frequency of second mode, TE_{02} , is around the operating frequency of vircator. This is also verified by applying procedure described in Section 3.3. Mode distribution along the z axis in both modulating cavity and output waveguide shows the distribution of TE_{01} in Figure 4.4 and 4.5.

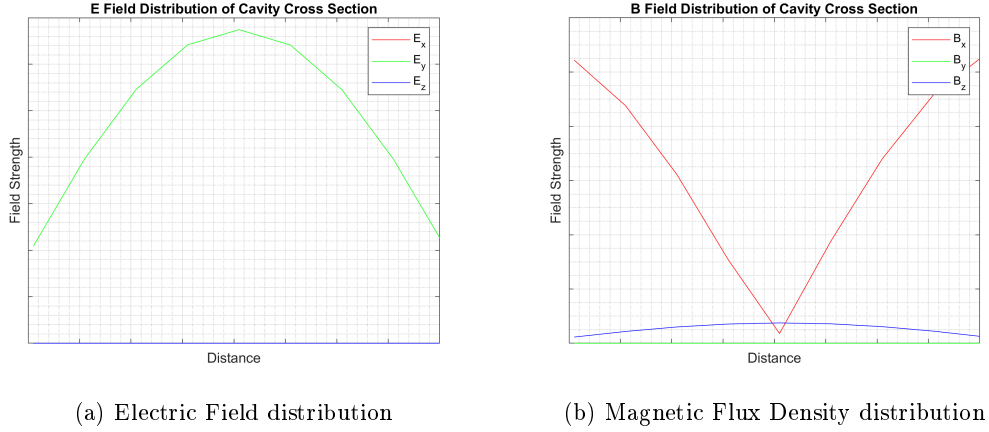


Figure 4.4: Field distribution at the modulating cavity

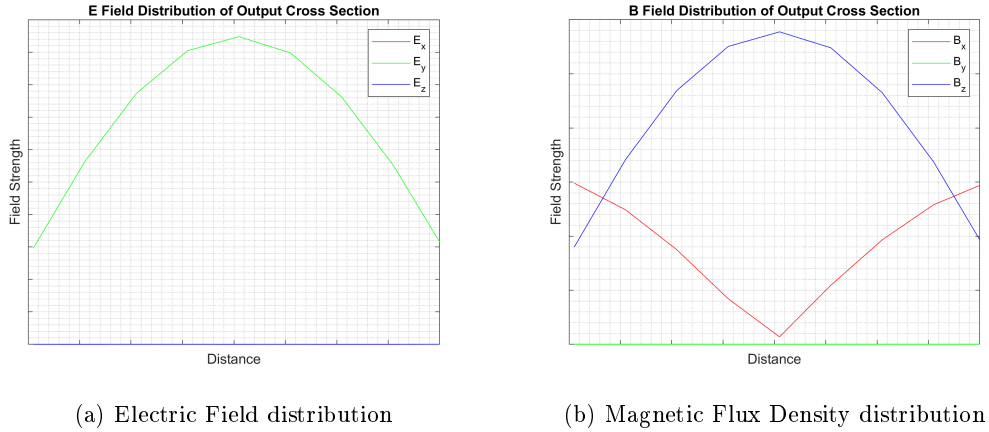


Figure 4.5: Field distribution at the output

Length of the modulating cavity is directly related to the coupled resonance mode. Since the length is threefold of the guided wavelength, TE_{106} resonance mode should be observed in modulating cavity. Electric field distribution for TE_{106} mode can be seen in Figure 4.6. Notice that standing wave maximum point is close to beam center. Figure 4.7 shows two sided field propagation at the output waveguide and one of them leads to modulation of electrom beam.

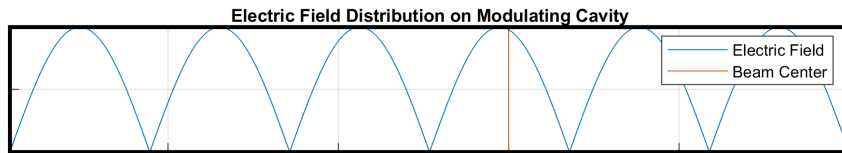


Figure 4.6: \bar{E} field distribution on modulating cavity

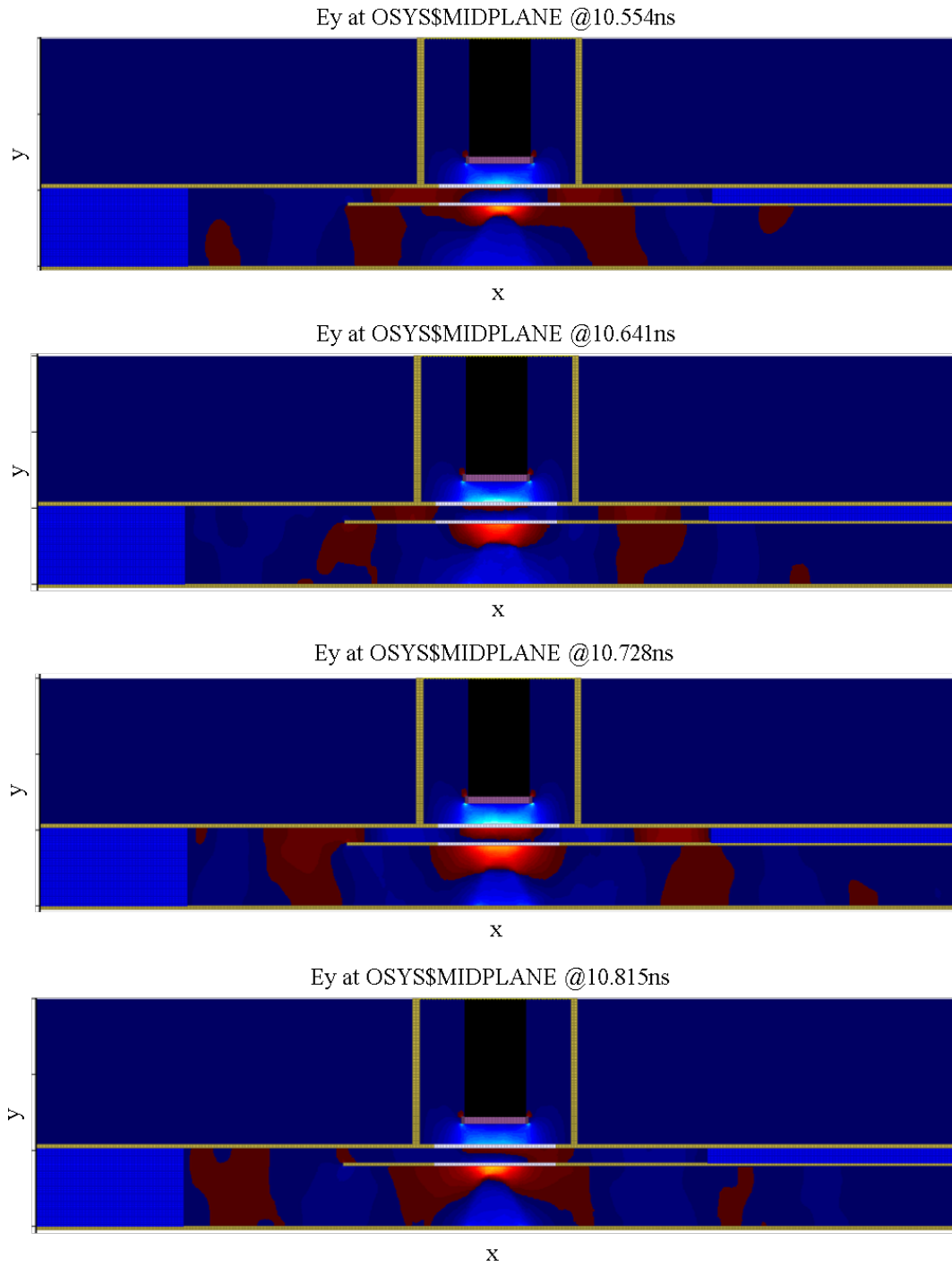


Figure 4.7: E_y at the midplane of vircator

Power efficiency is calculated for this thesis by using the peak value of the output power and mean value of the input power in the time interval of the flat region of the input voltage waveform. Energy efficiency is calculated from power results by using Matlab.

Coupled fields are obtained at the middle plane in z axis according to Figure 4.1. From these coupled fields, feedback of the generated fields to the modulating cavity can be observed. In order to determine the field strength at the cavity, E_y is measured along black line in Figure 4.9b, at the maximum point of the longitudinal field distribution of resonance mode and it is given in Figure 4.8. According to this figure, maximum peak to peak field strength of the coupled fields are approximately 70 MV/m.

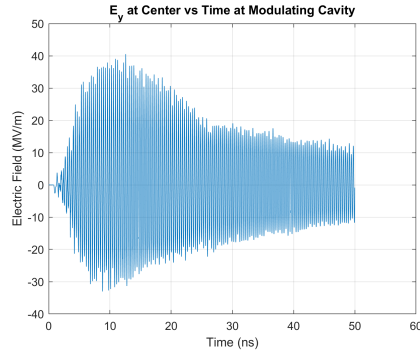


Figure 4.8: \bar{E}_y field variation in time at modulating cavity

4.1 Field Injection

In order to mimic the coupled fields into cavity, TE_{10} mode is injected into modulating cavity of the structure from the end of the small plunger shown in Figure 4.1. Field injection is done in Magic by specifying the field distributions of the desired mode and its time-dependent envelope function in PORT command. Figure 4.9 shows the injected TE_{106} distribution. Now let the location of the injection port shown in Figure 4.9a be $x = 0$ and edge of the large plunger be $x = l$ where l is the length of the cavity. Injected electric field is given in Equation 4.1 if y and z values of the lower left corner in Figure 4.9b is accepted as zero.

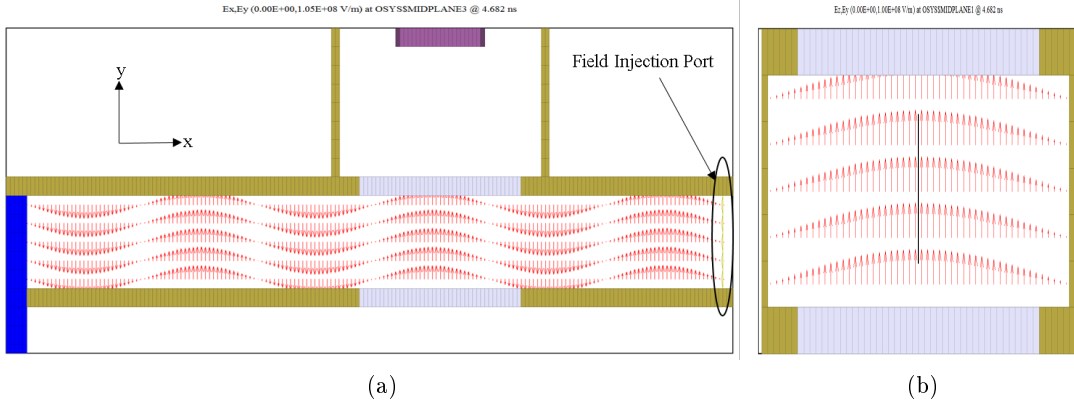


Figure 4.9: Cross sections of the modulating cavity under TE_{10} mode injection (a)longitudinal (b)transverse

$$E_y^{inc} = A_{10} \frac{\beta_z}{\epsilon} \sin(\beta_z z) e^{-j\beta_x x} \quad (4.1)$$

Since the reflection coefficient due to large plunger is -1 , total field in the cavity is found as in Equation 4.2.

$$E_y^{tot} = E_y^{inc} + E_y^{ref} = -2jA_{10} \frac{\beta_z}{\epsilon} \sin(\beta_z z) \sin(\beta_x x) \quad (4.2)$$

Applying boundary condition at the plunger surface, $\beta_x = \frac{p\pi}{l}$ is found where p is the integer number. In this case, resonance mode is called as TE_{10p} . Since the β_x is a frequency dependent parameter, correct resonance mode can be arranged by using the length of the cavity, l . In this case, resonance mode distribution is preserved as long as the injection continues. In addition, modulation of the beam by external electric field is expected to give earlier microwave generation since it removes microwave feedback delay from output waveguide. Vector plots in Figure 4.9 verifies the correct formation of resonance mode. Besides, this case can be considered as the driven of vircator by other microwave source. Average injection power is calculated from the injected signal. Injected signal is measured by along the black line in Figure 4.9b. This electric field measurement gives highest value of the E_y along z direction. In this time domain measurement, max value in the first few cycle is taken and named as E_0 . Theoretical value of E_0 can be found from Equation 4.1 and it is given in Equation 4.3.

$$E_0 = A_{10} \frac{\beta_z}{\epsilon} = A_{10} \frac{\pi}{a} \frac{1}{\epsilon} \quad (4.3)$$

where, a is the dimension of the cavity cross section along z . Time-averaged power flow of TE_{10} mode is given in Equation 4.4. Injected field power is calculated by this equation in Matlab.

$$P_{TE_{10}} = \frac{|A_{10}|^2 \pi^2}{2} \frac{1}{a^2} \frac{\beta_x}{\epsilon^2} \frac{ab}{w\mu} \frac{ab}{2} = \frac{|E_0|^2}{2} \frac{\beta_x}{w\mu} \frac{ab}{2} = \frac{|E_0|^2}{2} \frac{1}{Z_{TE}} \frac{ab}{2} \quad (4.4)$$

where, Z_{TE} is the wave impedance, b is cavity cross section dimension along y . Calculated time-average powers are also compared and verified with the average power measurement in Magic.

4.1.1 Feedback Disable

Table 4.1 gives average input parameters for each simulation. Approximately same input values are applied. First row of Table 4.2 shows the results of main structure giving at the beginning of this chapter. Other rows in the table shows field injection cases. Geometrically, small plunger is replaced with injection port shown in Figure 4.10 for aim of field injection.

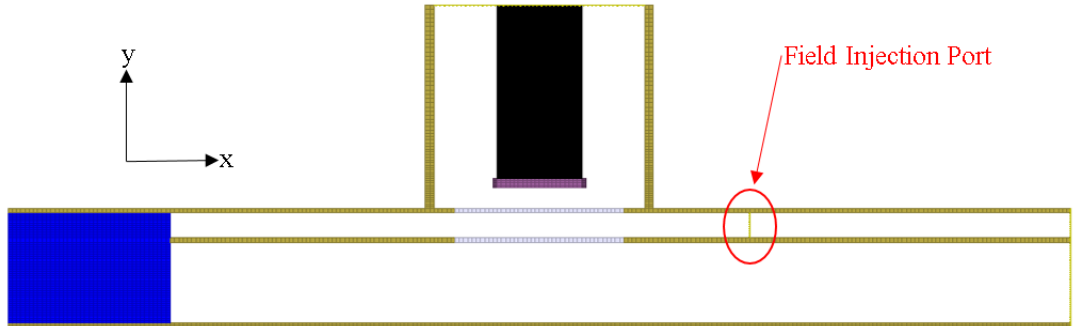


Figure 4.10: Viricator x-y cut with field injection port

Table4.1: Input parameters for injected field power without feedback

Input Voltage (kV)	Emitted Current (kA)	Input Power (GW)	Input Pulse Energy (J)
450.18	6.73	3.04	41.93

Main aim of this part is to mimic the coupled fields into modulating cavity. RF signals with same frequency and varying signal amplitude are injected to

Table 4.2: Results for varying injected field power without feedback

Injected Field Power (MW)	Peak Output Power (MW)	Output Field Energy (J)	Peak Output Power Efficiency (%)	Energy Efficiency (%)	Peak Power Total Efficiency (%)
–	406.65	1.36	13.44	3.27	13.44
0.16	110.95	0.25	3.68	0.60	3.68
4.86	209.24	0.83	6.89	1.97	6.88
16.02	306.52	1.20	10.08	2.84	10.02
33.66	359.00	1.62	11.77	3.85	11.64
57.89	421.34	1.95	13.81	4.64	13.56
88.35	435.32	2.22	14.30	5.30	13.89
125.04	467.02	2.44	15.36	5.82	14.75
170.20	487.76	2.80	16.07	6.72	15.22

the cavity by disabling feedback. Signal amplitudes are determined according to found coupled signal level in Figure 4.8. Feedback is disabled by closing coupling window shown in Figure 4.10. Figure 4.11a shows the spectrum for each case. Frequency of oscillation is preserved and frequency locking is observed. Output power graphs are given in Figure 4.11b and earlier generation of microwaves about 4 ns is obtained for external field injection cases. However, the cases of lower power injection has earlier decay in output power curves which is not completely understood. For this values, proper modulation might not be reached due to lower power injection [66]. Table 4.2 shows the results of the field injection case without internal feedback. Results in the first column is the time-average power. Peak power total efficiency in the last column is obtained by adding the average injected field power to the denominator of power efficiency calculation. For the average injected power of 33.66 MW, energy efficiency is caught the one in first row belongs to main case due to earlier start of microwave generation. This injected power value corresponds to the case of driven of vircator with 18.8% percent of its peak output power. For the average injected power of 57.89 MW, peak power total efficiency exceeds the value of main case. Now, in this case vircator is driven by 27.5% of its peak power.

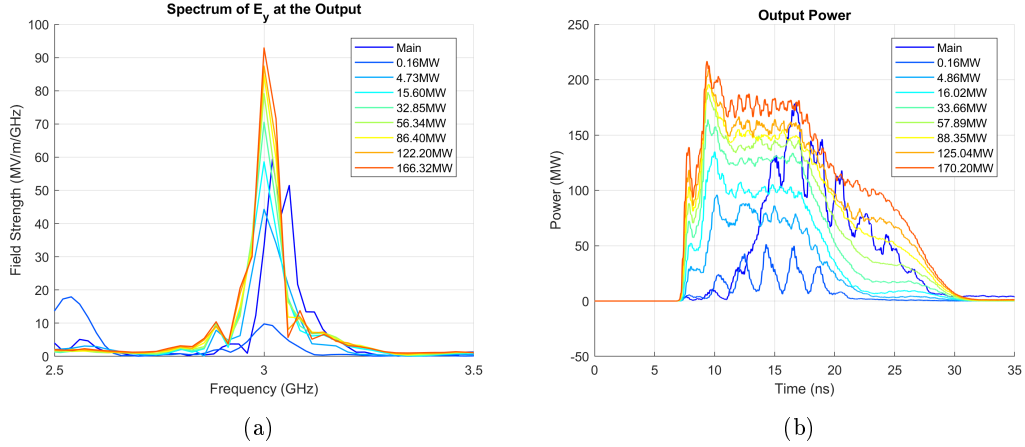


Figure 4.11: (a) Spectrum of generated EM fields (b) Output microwave power (filtered by step filter with a period of generated wave)

4.1.1.1 Frequency Shifts

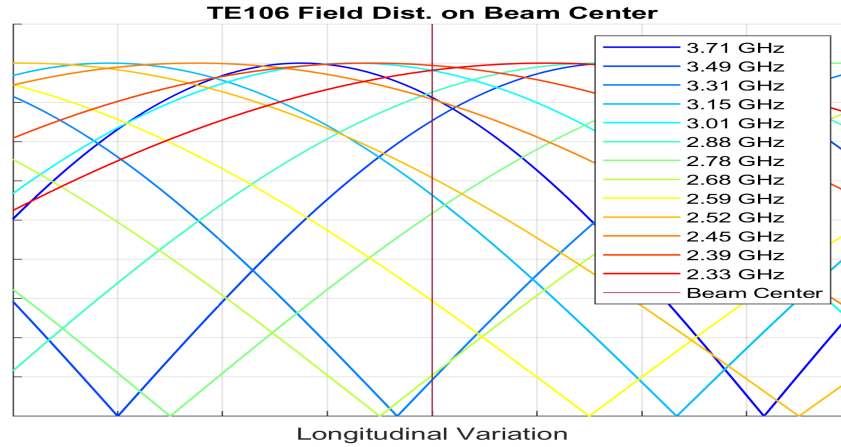


Figure 4.12: TE_{106} mode distributions on the beam center

Frequency locking capability of the vircator is tested in this section with a configuration given in Figure 4.10 . While injected field power is keeping constant as 57.89 MW in Table 4.2, frequency of the injected signal is varying. By arranging the length of cavity at each simulation, correct TE_{106} mode distribution is formed in the modulating cavity. However, this results in distribution variation around beam center as shown in Figure 4.12. Figure 4.13 gives the frequency spectrum for each simulation. Table 4.3 and 4.4 shows input parameters and output results for each simulation respectively. The results for 2.68 GHz and

Table4.3: Input parameters for field injection with different frequencies without feedback

Input Voltage (kV)	Emitted Current (kA)	Input Power (GW)	Injected Field Power (MW)	Input Pulse Energy (J)
450.18	6.74	3.04	57.80	42.07

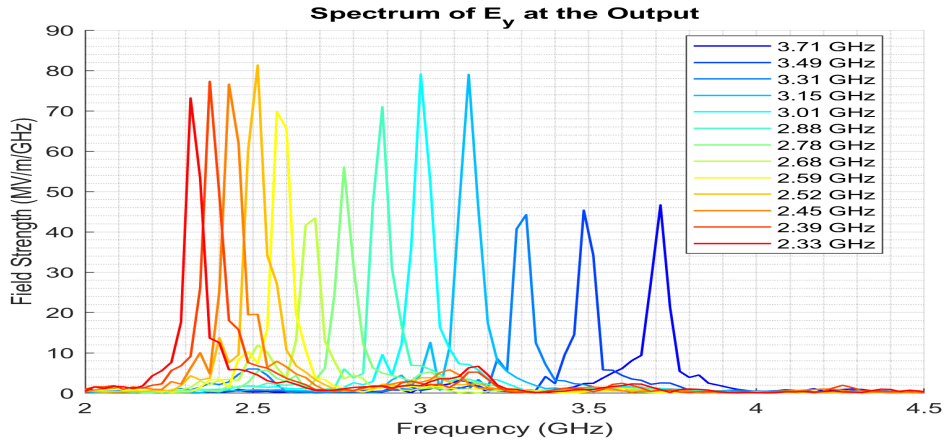


Figure 4.13: Output spectrum of generated electromagnetic fields

Table4.4: Results for field injection with different frequencies without feedback

Injection Frequency (GHz)	Peak Output Power (MW)	Output Field Energy (J)	Peak Output Power Efficiency (%)	Energy Efficiency (%)	Peak Power Total Efficiency (%)
3.71	165.20	0.74	5.46	1.77	5.36
3.49	115.37	0.73	3.81	1.75	3.74
3.31	144.45	0.77	4.74	1.83	4.66
3.15	373.24	2.00	12.14	4.72	11.92
3.01	421.34	1.95	13.81	4.64	13.56
2.88	229.54	1.54	7.50	3.66	7.37
2.78	193.43	0.94	6.32	2.22	6.20
2.68	167.56	0.82	5.49	1.93	5.39
2.59	287.67	1.82	9.39	4.29	9.22
2.52	360.42	2.24	11.83	5.33	11.61
2.45	418.24	2.05	13.84	4.89	13.58
2.39	406.89	1.79	13.46	4.28	13.21
2.33	295.35	1.64	9.76	3.91	9.58

3.31 GHz injection case, shows the distinguishable efficiency drop. The reason of this is its lower field value around the beam center shown in Figure 4.12. Al-

though higher field value in beam center is theoretically expected for 3.71 GHz and 3.49 GHz injection cases, their efficiency values is as low as 2.68 GHz and 3.31 GHz cases. Reasoning will be given in the next section.

4.1.1.1.1 S Band Frequency Locking

In order to investigate the efficiency decrease observed in previous section for higher frequencies, TE_{103} mode is injected to the system for various frequencies in S band for given average input parameters in Table 4.5. Figure 4.10 is used for this part also. All cases approximately same field strength and their longitudinal variation of each case is given in Figure 4.14. According to this figure, standing wave maximum points for each injection is at the beam center of the modulating cavity.

Table4.5: Input parameters for S band field injection with different frequencies without feedback

Input Voltage (kV)	Emitted Current (kA)	Input Power (GW)	Injected Field Power (MW)	Input Pulse Energy (J)
450.18	6.71	3.02	50.57	41.79

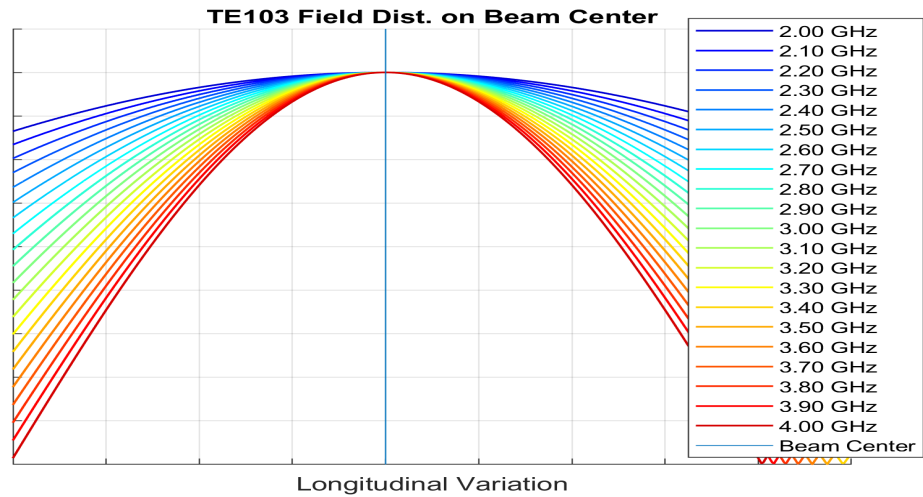


Figure 4.14: TE_{103} mode distributions on the beam center

Figure 4.15a shows the frequency locking ability of the device in S band. Figure

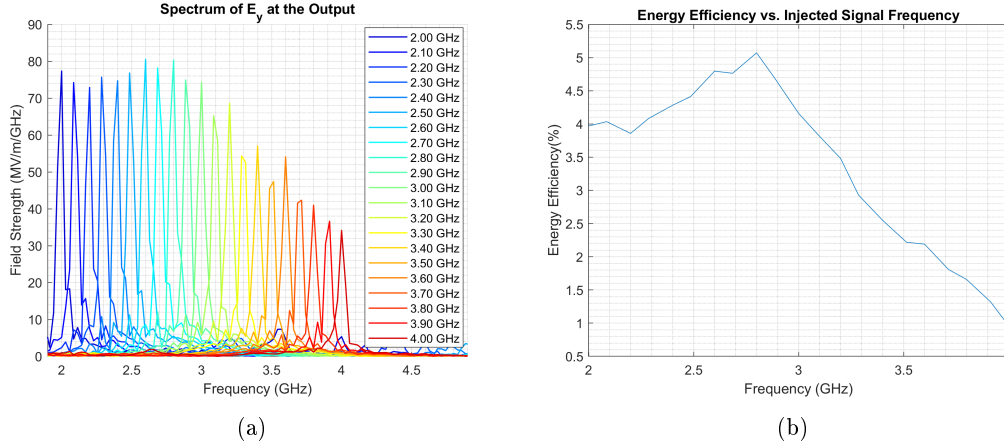


Figure 4.15: (a) Output spectrum of generated electromagnetic fields (b) Output spectrum of generated electromagnetic fields

4.15b indicates the total energy efficiency values of each case. According to this figure, efficiency starts to decrease for larger frequencies of injection. The reason of this can be explained from Figure 4.14. For larger frequency values, half of the guided wavelength becomes comparable to the beam diameter and this prevents uniform modulation of electron beam.

4.1.1.2 Injection Input Phase Delay

For the same frequency and amplitude of injection, effect of phase delay is examined. Injected field power is keeping constant as 57.89 MW in Table 4.2 and frequency of injection is applied to Figure 4.10. Phases of the input signals are shifted by using the temporal function of PORT command. Figure 4.16a shows injected signal at the port. Figure 4.16b gives the y component of the electric field at the waveguide output. Phases of the output signal are shifted also accordingly and this gives the phase locking behavior of the device to injected signal.

4.1.1.3 Cavity Field Distribution

For a constant cavity length, location of the maximum of cavity fields along longitudinal direction is investigated in this part. Used geometry is given in

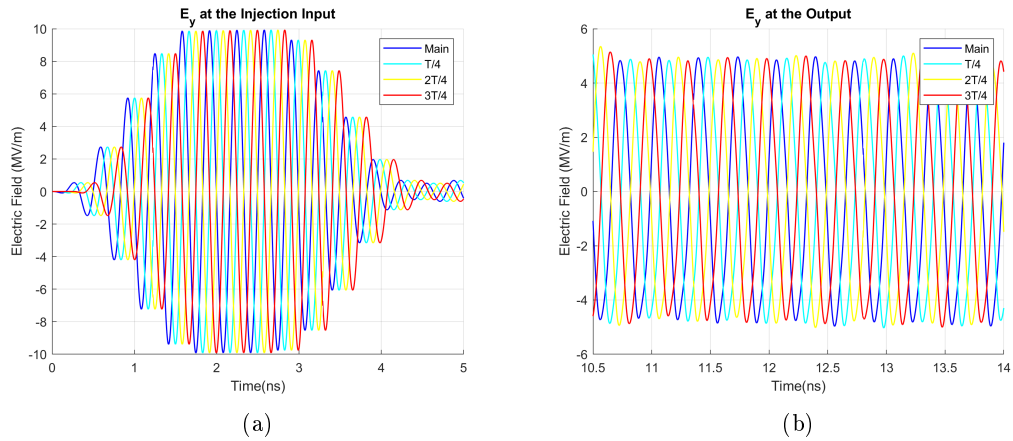


Figure 4.16: (a)Time delayed injected signals (b)Output signals

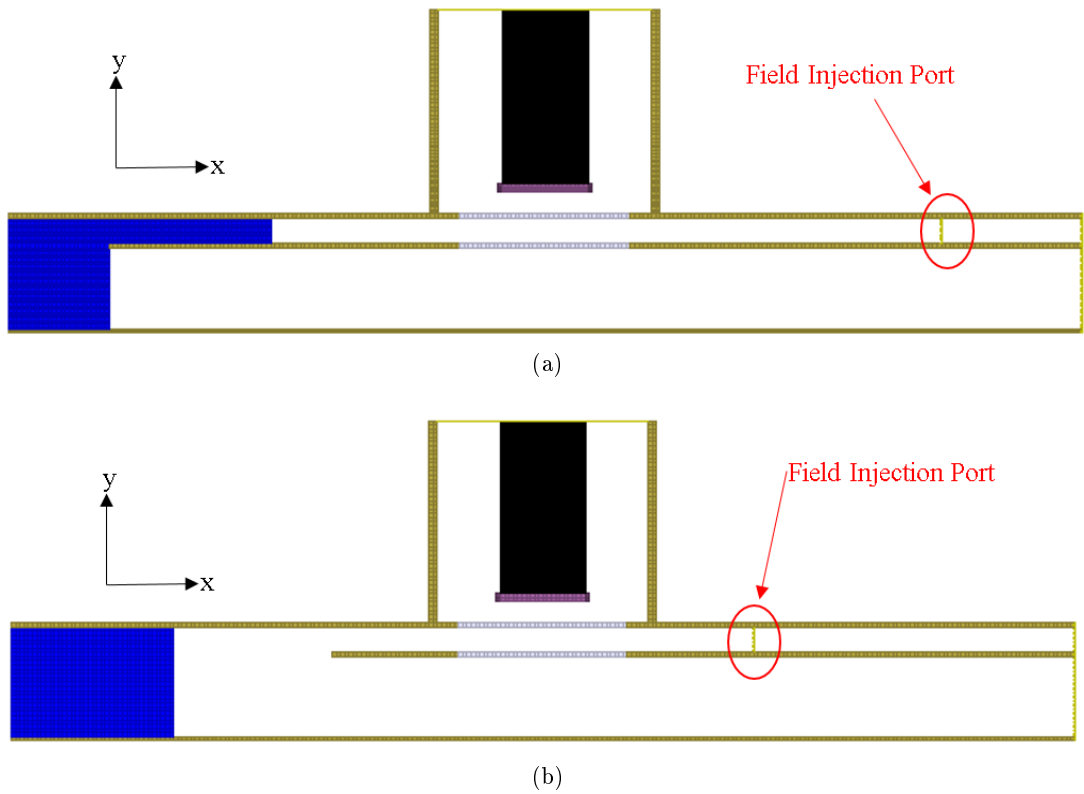


Figure 4.17: (a)Geometry for cavity field distribution test under external field (b) Vircator x-y cut with enabling feedback

Figure 4.17a. In this geometry, field injection port and plunger is shifted with the same amount when injected frequency is keeping same in Section 4.1.1. By this way, different field quantities are formed at the beam center and effect of the field distribution of cavity to modulation of the beam and also microwave generation is observed. Input parameters are similar to values given in Table 4.3.

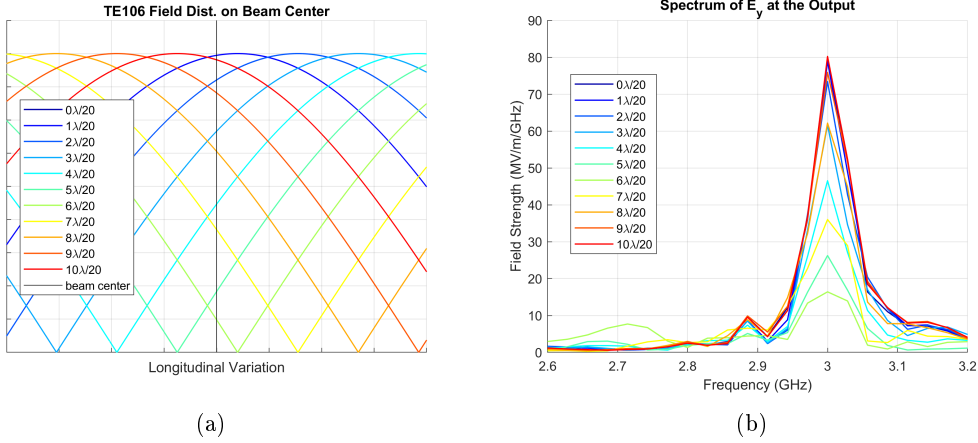


Figure 4.18: (a)Cavity field distributions (b) Output spectrum

Table 4.6: Results for field injection for constant cavity length without feedback

Shift of Cavity (λ_g)	Peak Output Power (MW)	Output Field Energy (J)	Peak Output Power Efficiency (%)	Energy Efficiency (%)	Peak Power Total Efficiency (%)
–	421.34	1.95	13.81	4.64	13.56
$\lambda_g/20$	417.64	1.90	13.70	4.53	13.44
$2\lambda_g/20$	401.40	1.70	13.11	4.03	12.87
$3\lambda_g/20$	309.34	1.25	10.09	2.96	9.91
$4\lambda_g/20$	176.89	0.77	5.78	1.83	5.67
$5\lambda_g/20$	85.62	0.33	2.81	0.79	2.75
$6\lambda_g/20$	79.24	0.25	2.60	0.59	2.55
$7\lambda_g/20$	162.19	0.60	5.30	1.42	5.20
$8\lambda_g/20$	295.62	1.38	9.63	3.26	9.45
$9\lambda_g/20$	390.87	1.89	12.77	4.48	12.53
$10\lambda_g/20$	423.00	2.00	13.89	4.76	13.63

Figure 4.18a shows the TE_{106} field distribution for each simulation. According to Table 4.6, efficiency decreases are strongly related to the given field distribution in Figure 4.18a. When the field value at beam center gets higher, increased microwave generation is observed which is resulted from the stronger modulation of beam. It is noticeable here that frequency of EM field at the output of the device is preserved as seen in Figure 4.18b.

4.1.2 Feedback Enable

Section 4.1.1 is repeated with enabling internal feedback mechanism of the device. Figure 4.17b shows the geometry used for this simulation. Similar input parameters in Section 4.1.1 are used and output results are given in Table 4.7. First row of Table 4.7 shows the results of main geometry. For all cases, slightly lower output values are obtained in Table 4.7 when it is compared to Table 4.2. Possible reason is the degeneration of the field distribution on cavity. Due to leak into output waveguide, reflection coefficient considered in Equation 4.2 will not be -1 any more.

Table4.7: Results for varying injected field with feedback

Injected Field Power (MW)	Peak Output Power (kV)	Output Field Energy (J)	Peak Output Power Efficiency (%)	Energy Efficiency (%)	Peak Power Total Efficiency (%)
–	406.65	1.36	13.44	3.27	13.44
0.16	78.57	0.17	2.61	0.41	2.61
4.80	201.74	0.85	6.64	2.03	6.63
15.82	257.87	1.16	8.47	2.77	8.43
33.23	326.11	1.49	10.71	3.55	10.59
57.16	366.12	1.79	12.06	4.28	11.83
123.45	397.39	2.21	13.15	5.31	12.64
168.03	412.85	2.53	13.71	6.13	12.98

Figure 4.19a and 4.19b shows the output spectrum of E_y and output power. As shown in Figure 4.19a, frequency is still locked to injected signal frequency even if the internal feedback is enabled. 4ns earlier generation of microwave is also observed in Figure 4.19b. From this point forward, no field is injected to cavity and field injection port is replaced with small plunger in Figure 4.1.

4.2 Coupling Window

In Ref. [62], it is stated that microwave output power has periodical dependence to the length of the coupling window. This information is tested with input

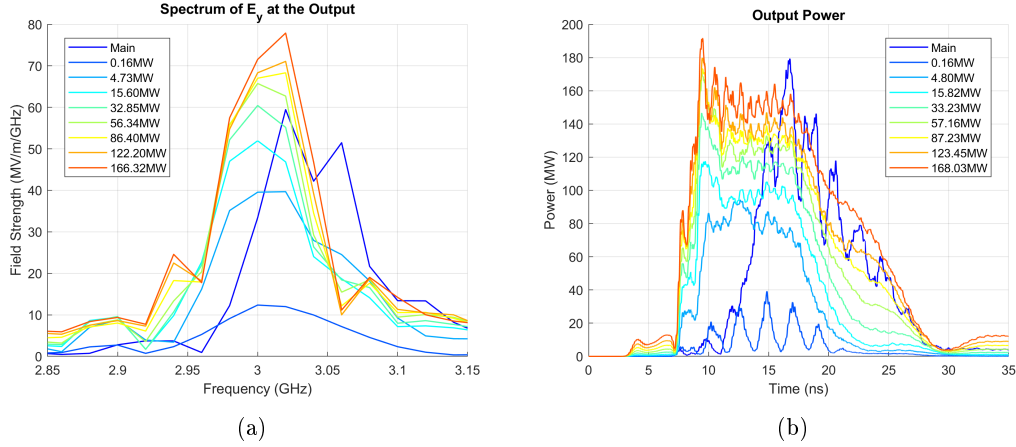


Figure 4.19: (a) Spectrum of generated EM fields (b) Output microwave power (filtered by step filter with a period of generated wave)

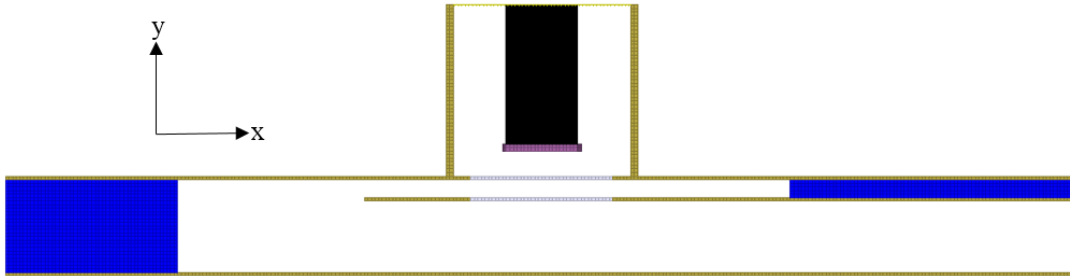


Figure 4.20: Main geometry of double gap vircator

parameters given in Table 4.1 with geometry given in Figure 4.20. Efficiency values with respect to shift of coupling window length is given in Figure 4.21. These graphs are verified the periodic dependence of the output power to size of the window over every half of guided wavelength shift.

4.3 Small Plunger

Table4.8: Input parameters for small plunger shift cases

Input Voltage (kV)	Emitted Current (kA)	Input Pulse Power (GW)	Input Pulse Energy (J)
450.18	6.59	3.05	42.41

Effect of small plunger is simulated with geometry in Figure 4.20. Since it determines the length of the cavity, it directly affects the resonance mode distribution

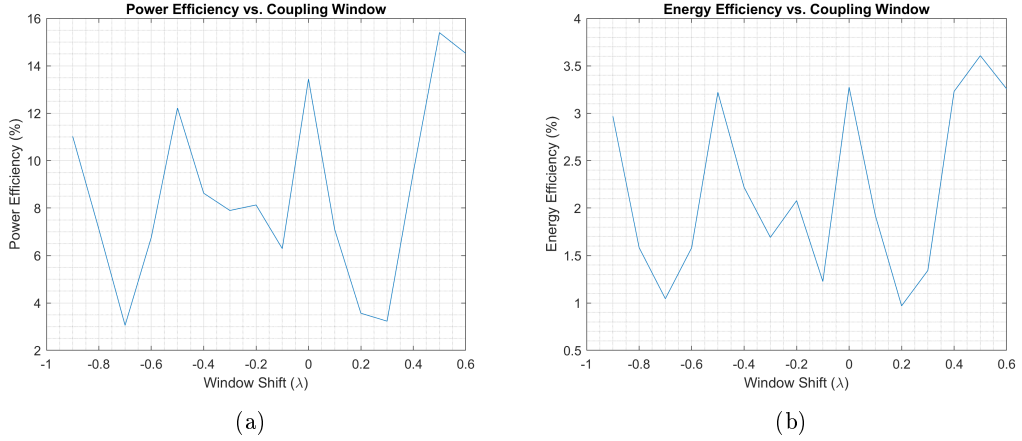


Figure 4.21: (a)Peak power efficiency vs. coupling window (b)Energy efficiency vs. coupling window

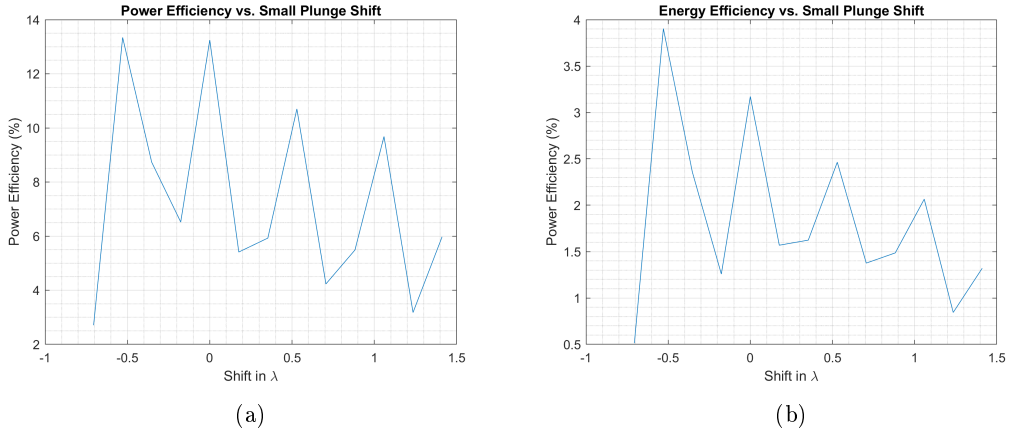


Figure 4.22: Efficiency vs position of small plunge (a)Peak power efficiency (b)Energy efficiency

formed in the cavity. Table 4.8 shows average input parameters and Table 4.9 shows results for all cases. First column in Table 4.9 gives shifting distance in terms λ_g calculated in no shift case. Also, last column shows the cavity lengths in λ_g in terms of frequency of operation for each simulation. Main frequency column in Table 4.9 indicates frequency that corresponds to maximum strength value in FFT of E_y at the waveguide output. Periodic behaviour of the efficiencies depending on the small plunge shift in every $\lambda_g/2$ shift is observed in Figure 4.22. Besides, this figure shows that the closer the small plunger to beam center is, the higher efficiency is obtained. For a every $\lambda_g/2$ shift of small plunger, resonance mode of the cavity is change from TE_{10p} to TE_{10m} for the same fre-

Table 4.9: Results for small plunger shift cases

Shift in Small Plunge (λ_g)	Peak Output Power (kV)	Output Field Energy (J)	Peak Output Power Efficiency (%)	Energy Efficiency (%)	Main Frequency (GHz)	Cavity Length (λ_g)
-0.71	82.66	0.22	2.71	0.51	2.56	1.83
-0.53	408.64	1.65	13.34	3.90	3.06	2.53
-0.35	266.59	1.00	8.73	2.36	2.88	2.50
-0.18	198.70	0.53	6.52	1.26	3.18	3.04
0	404.16	1.33	13.25	3.17	3.02	3.01
0.18	164.99	0.67	5.41	1.57	2.88	2.99
0.35	180.54	0.69	5.93	1.62	3.14	3.54
0.53	326.18	1.04	10.70	2.46	3.00	3.51
0.71	128.87	0.58	4.23	1.38	2.88	3.48
0.88	167.20	0.63	5.49	1.49	3.10	4.02
1.06	294.84	0.87	9.68	2.07	2.98	3.99
1.24	96.70	0.36	3.18	0.84	2.88	3.97
1.41	181.85	0.56	5.97	1.32	3.08	4.53

quency. Note that p and m are consecutive integer numbers. Table 4.9 indicates this periodic behaviour. Rows of Table 4.9 with a plunge shift of $-0.53\lambda_g$, $0\lambda_g$, $0.53\lambda_g$ and $1.06\lambda_g$ describes change of resonance mode of cavity at the same frequency. Resonance mode is altered from TE_{105} to TE_{108} with these shifts. This behaviour is also mentioned in Ref. [4].

4.4 Large Plunger

Effect of large plunger is examined by shifting it in the amount of $\lambda_g/40$ steps. Input parameters are similar to values given in Table 4.8. Table 4.10 includes output results. First column in Table 4.10 shows the shift of large plunger λ_g according to main case. Last column of Table 4.10 shows the possibility of fine tuning of the frequency of operation, even if there is efficiency decreases beyond the main case. As can be seen in Figure 4.23, no nulls of the field distribution is formed around beam center.

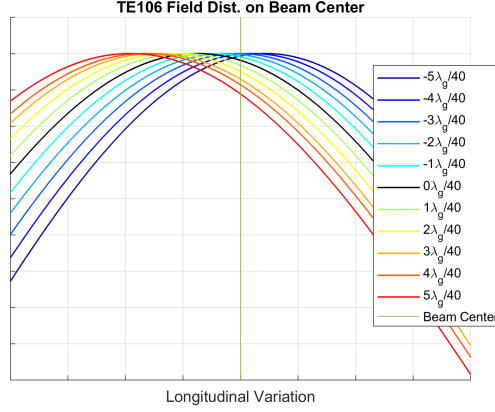


Figure 4.23: Field distribution around beam center

Table 4.10: Results for position of large plunger shift cases

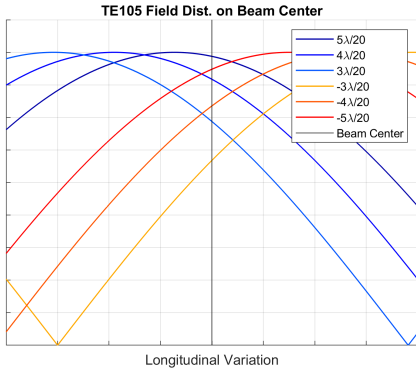
Shift in Plunger Position (λ_g)	Peak Output Power (MW)	Output Field Energy (J)	Peak Output Power Efficiency (%)	Energy Efficiency (%)	Frequency (GHz)
$5\lambda_g/40$	291.73	1.08	9.63	2.60	3.14
$4\lambda_g/40$	296.73	1.12	9.80	2.68	3.11
$3\lambda_g/40$	355.65	1.22	11.76	2.95	3.09
$2\lambda_g/40$	377.83	1.26	12.49	3.04	3.06
$1\lambda_g/40$	431.07	1.37	14.26	3.31	3.06
Main	406.65	1.36	13.44	3.27	3.02
$-1\lambda_g/40$	445.66	1.37	14.72	3.29	3.00
$-2\lambda_g/40$	444.26	1.36	14.69	3.26	3.00
$-3\lambda_g/40$	410.74	1.21	13.57	2.90	2.97
$-4\lambda_g/40$	346.47	1.03	11.45	2.45	2.94
$-5\lambda_g/40$	246.91	0.86	8.17	2.04	2.91

4.4.1 Constant Cavity Length

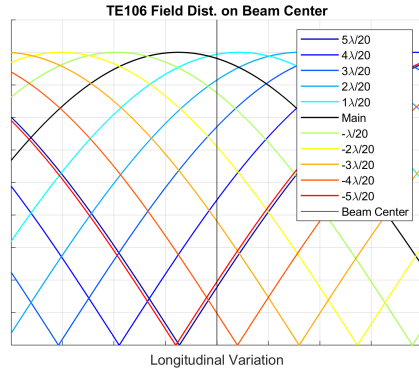
In this part, aim is to investigate the cavity field distribution with a constant cavity length for the geometry in Figure 4.20. Input parameters are similar to given in Table 4.8. By keeping the cavity length same, both small and large plunger are positioned in region of quarter guided wavelength found in the main case. However in this case, some field distributions have lower values near the beam center. Measured frequency for the first and last three row in Table 4.11 shows different frequency than the other rows. For these rows, field distribution

Table 4.11: Results for constant cavity length with feedback

Shift of Both Plungers (λ_g)	Peak Output Power (MW)	Output Field Energy (J)	Peak Output Power Efficiency (%)	Energy Efficiency (%)	Frequency (GHz)
$5\lambda_g/20$	189.23	0.46	6.28	1.09	2.60
$4\lambda_g/20$	141.64	0.41	4.70	0.98	2.66
$3\lambda_g/20$	87.72	0.29	2.91	0.69	2.63
$2\lambda_g/20$	224.88	0.93	7.44	2.24	3.03
$1\lambda_g/20$	363.19	1.18	12.00	2.85	3.03
Main	406.65	1.36	13.44	3.27	3.02
$-1\lambda_g/20$	398.06	1.07	13.16	2.57	3.03
$-2\lambda_g/20$	189.43	0.50	6.26	1.20	3.03
$-3\lambda_g/20$	103.01	0.28	3.41	0.67	2.60
$-4\lambda_g/20$	132.47	0.43	4.38	1.02	2.60
$-5\lambda_g/20$	154.56	0.54	5.12	1.30	2.60



(a) TE_{105} field distribution



(b) TE_{106} field distribution

Figure 4.24: Resonant mode field distribution in modulating cavity

of TE_{105} , which is shown in Figure 4.24a, dominates the beam modulation and as a result, frequency of output EM fields are changed. Importance of the field distribution on the cavity beam center is observed for the geometry in Figure 4.20. In order to satisfy the condition of maximization of field distribution on beam center, distance between beam center and any of plunger must odd number multiples of quarter guided wavelength of desired frequency. This condition is already used in the Ref. [28, 29, 54]. In addition to findings in Section 4.1.1.3, this part indicates that some other modes can be coupled to cavity if the field

distribution of desired mode is not enough to modulate the beam.

4.5 Foil Transmission Fraction

Anode is an important component of the vircator when its transparency, its effect of gap closure and heat resistibility is considered. All these have effects on output microwave duration and repeatability of vircator. In this part, anode transparency is tested with main geometry in Figure 4.20. Similar input parameters to the ones in Table 4.8 are used to simulate the structure with different foil transparency levels given in first column of Table 4.12. Figure 4.25a and efficiency columns in Table 4.12 shows strong dependency of output power on the foil transparency. Nevertheless, frequency is preserved as indicated in Figure 4.25b although lower efficiencies are observed. Foil thickness in these simulations are $200\mu m$. It is known from the Table 3.2 and Table 3.3 that for $200\mu m$ foil thickness, only possible electron transition beyond foil is the ones passing foil undeflected which is direct parameter of FTF. To further increase the passing electron density beyond foil, higher electron beam energy or thinner foil is required when Magic simulation is considered. Experimental studies show that mesh anodes whose transparencies are higher than 0.9 and foil anodes whose thicknesses are lower than $50\mu m$ are preferred for this vircator geometry [28, 83]. In Ref. [83], best result is obtained with $5\mu m$ foil anodes.

Table4.12: Results for different foil transmission fraction values

Foil Transmission Fraction	Peak Output Power (MW)	Output Field Energy (J)	Peak Output Power Efficiency (%)	Energy Efficiency (%)
0.9	4.44	0.02	0.15	0.04
0.92	14.93	0.05	0.49	0.12
0.94	46.76	0.16	1.53	0.38
0.96	154.26	0.55	5.07	1.32
0.98	341.08	1.13	11.23	2.70
1	406.65	1.36	13.44	3.27

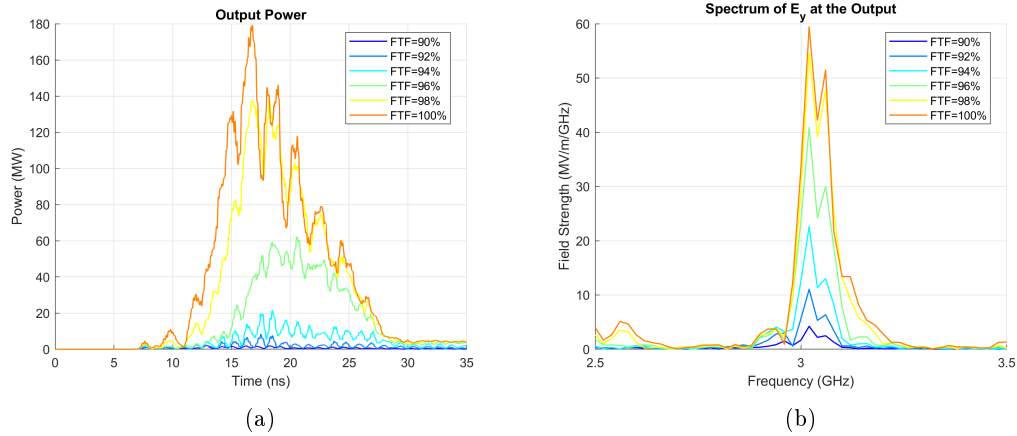


Figure 4.25: (a) Output power (filtered by step filter with period of generated wave) (b) electromagnetic spectrum of outgoing field

4.6 Natural Oscillation Frequencies and Tuning Procedure

From Figure 4.7, it is shown that there is a feedback from the output waveguide to modulating cavity. In Section 4.1.1.3, perfect cavity is investigated under external signal and maximization of field at beam center gives higher output power. In Section 4.4.1, similar condition is tested and it is observed that when field distribution is minimized around beam center other cavity modes might be observed. In addition, periodic effect of coupling window in terms of guided wavelength is seen in Section 4.2. In the light of these learning outcomes, device could be tuned according to the generated frequency at the output waveguide. In order to predict frequency of generation at the output waveguide, some modifications are applied to geometry as shown in Figure 4.26.

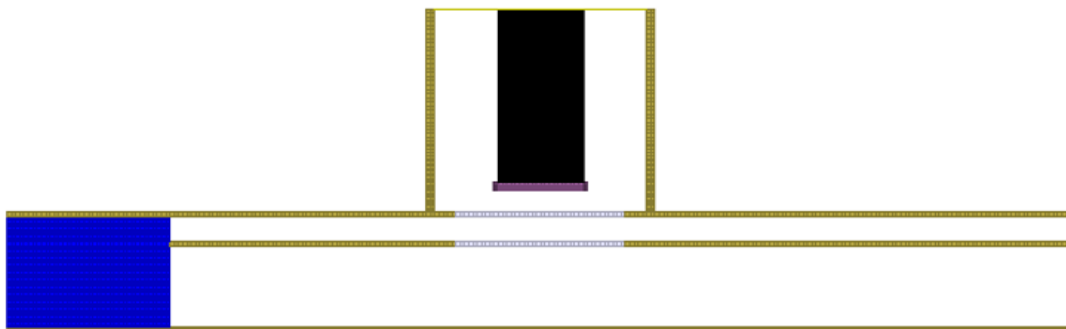


Figure 4.26: Tuning geometry used for finding natural oscillation frequencies

Since the frequencies result from electron movement is desired, modulation of the beam is tried to minimized. To achieve minimum modulation, coupling window is closed and small plunger is replaced with port located at the end of the device. By this way, coupling from output waveguide is ceased and fields formed due to beam in the cavity is enabled to leave via port. Frequency of generation found by using this geometry will be called as natural oscillation frequency. Natural oscillation frequencies for main geometry is found as in Figure 4.27.

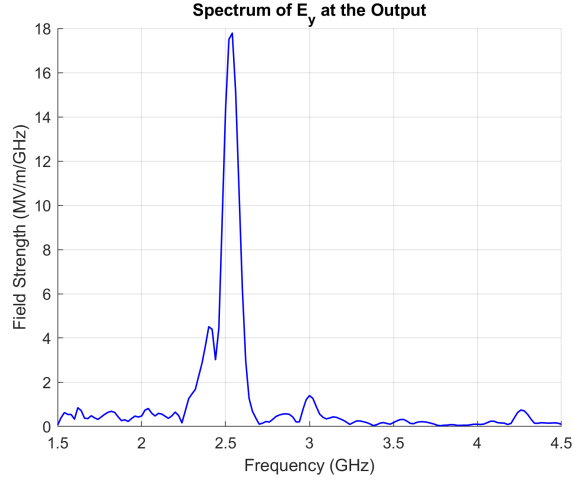


Figure 4.27: Electromagnetic spectrum of outgoing field

Procedures for tuning is itemized as follows:

1. Determining the natural oscillation frequencies. In this step, microwave mode should also be verified to be TE_{10} .
2. Specifying the position of large plunger such that it should leads to cavity field maximization at beam center. From the frequency found in item 1, guided wavelength is calculated. Required distance between large plunger and beam center must be odd multiples of quarter of calculated quided wavelength.
3. Locating the small plunger such that desired resonance mode for the frequency of interest must be formed. Length of the cavity should be integer multiples of half of the guided wavelength.
4. Optimizing the size coupling window by using its periodical behavior over half of guided wavelength.

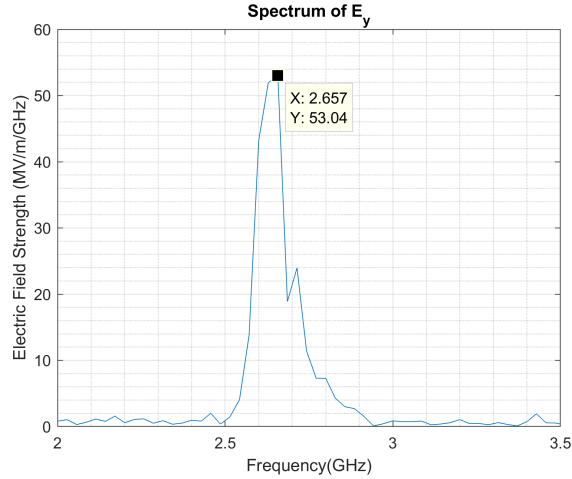


Figure 4.28: Output spectrum for 2.56GHz tuning procedure

4.6.1 Tuning to 2.56GHz in Main Geometry

Table 4.13 includes the results after applying the tuning procedure to frequency given in Figure 4.27. As a heighest, 14.39% peak power efficiency and 4.2% energy efficiency is obtained at 2.66 GHz operation frequency. Efficiency values for the main geometry was 13.44% and 3.27% in terms of peak power and energy respectively. Spectrum for the best result in Table 4.13 is given in Figure 4.28.

Table4.13: Results for tuning procedure to main geometry

Shift of Coupling Window (λ_g)	Peak Output Power (MW)	Output Field Energy (J)	Peak Output Power Efficiency (%)	Energy Efficiency (%)	Frequency (GHz)
–	104.20	0.35	3.46	0.83	2.57
$-1\lambda_g/20$	21.64	0.08	0.72	0.19	2.49
$-2\lambda_g/20$	136.35	0.35	4.51	0.84	2.77
$-3\lambda_g/20$	141.93	0.44	4.67	1.06	2.74
$-4\lambda_g/20$	211.75	0.74	6.95	1.76	2.74
$-5\lambda_g/20$	312.35	1.33	10.26	3.18	2.69
$-6\lambda_g/20$	436.89	1.75	14.39	4.20	2.66
$-7\lambda_g/20$	396.37	1.64	13.09	3.93	2.60
$-8\lambda_g/20$	240.37	1.15	7.97	2.75	2.60
$-9\lambda_g/20$	158.28	0.64	5.25	1.53	2.54

4.6.2 Tuning Procedure for 750kV Peak Input Voltage

Peak value of input voltage waveform is risen to 750 kV and tuning procedure is tested for this case. Average input parameters for every simulation is given in Table 4.14. Obtained output results for the main geometry in Figure 4.20

Table4.14: Inputs for 750kV for application

Input Voltage (kV)	Emitted Current (kA)	Input Pulse Power (GW)	Input Pulse Energy (J)
749.82	13.46	10.15	142.00

Table4.15: Results for 750kV application

	Peak Output Power (MW)	Output Field Energy (J)	Peak Output Power Efficiency (%)	Energy Efficiency (%)	Frequency (GHz)
Main Geometry	1037.60	3.35	10.22	2.36	3.77
Tuning Geometry	1285.68	4.98	12.79	3.56	3.71

and tuning geometry in Figure 4.26 before the application of tuning procedure is given in Table 4.15 in the first and second row respectively. Figures 4.29

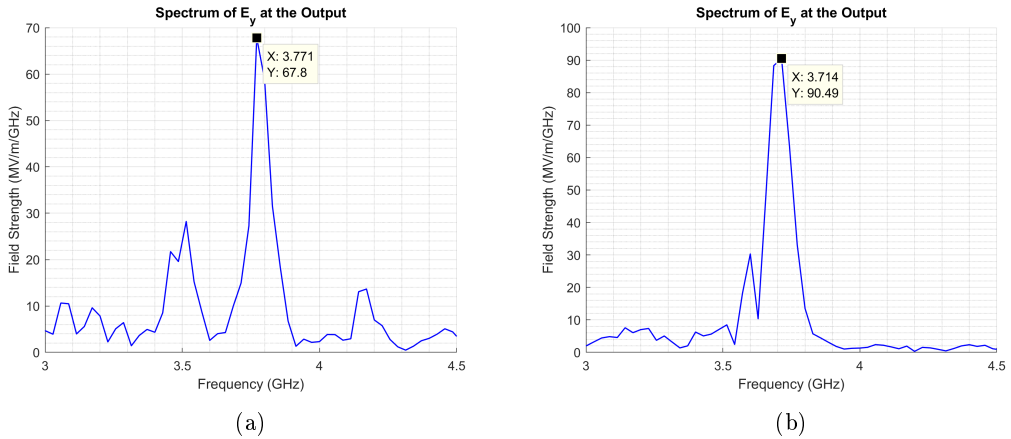


Figure 4.29: (a)Output spectrum for main structure (b)Output spectrum shows natural oscillation frequencies

shows the output spectrums of main structure with 750 kV applied voltage and

found natural frequencies for 750 kV application as an input. Tuning procedure is applied according to frequency component given in Figure 4.29b. Before applying the tuning procedure, generated mode is verified as TE_{10} in Figure 4.30. Table 4.16 gives the output results after applying the tuning procedure.

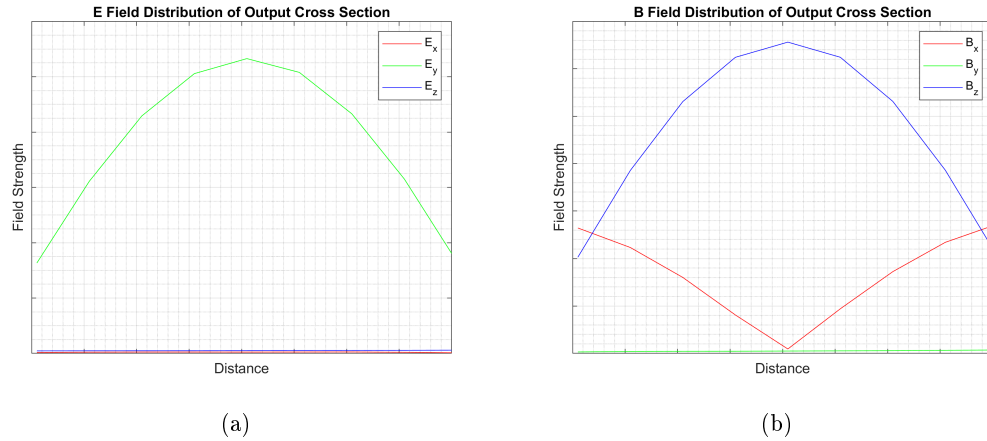


Figure 4.30: Field distribution for 750kV application

Rows indicated with bold text shows best result. According to this result, energy efficiency is increased to 5.22 % according to both efficiency value in Table 4.15.

Table4.16: Results after tuning procedure for 750 kV

Shift of Coupling Window (λ_g)	Peak Output Power (MW)	Output Field Energy (J)	Peak Output Power Efficiency (%)	Energy Efficiency (%)	Frequency (GHz)
–	1263.76	6.76	12.52	4.84	3.74
$-1\lambda_g/20$	1397.20	6.94	13.94	4.99	3.74
$-2\lambda_g/20$	1369.09	7.13	13.60	5.12	3.74
$-3\lambda_g/20$	1670.21	7.03	16.56	5.03	3.74
$-4\lambda_g/20$	1617.97	7.29	16.11	5.22	3.74
$-5\lambda_g/20$	1416.00	6.95	14.08	4.99	3.71
$-6\lambda_g/20$	1386.62	6.52	13.77	4.68	3.71
$-7\lambda_g/20$	1432.36	6.09	14.23	4.33	3.71
$-8\lambda_g/20$	1391.26	4.04	13.81	2.86	3.71
$-9\lambda_g/20$	1284.42	3.73	12.68	2.63	2.69
$-10\lambda_g/20$	1233.20	3.82	12.18	2.70	3.94

4.6.3 Tuning Procedure for Different AK Gap Distances

4.6.3.1 11mm AK Gap Distance

For 11mm AK gap distance, results of main geometry in Figure 4.20 and tuning geometry in Figure 4.26 which is used to find natural oscillation frequency of the system is given in Table 4.17. Energy efficiency for main geometry is 2.74% and frequency of operation is found as 3.74 GHz. Tuning procedure is applied for 3.62 GHz natural oscillation frequency given in Table 4.17.

Table4.17: Results for 11mm AK gap

	Peak Output Power (MW)	Output Field Energy (J)	Peak Output Power Efficiency (%)	Energy Efficiency (%)	Frequency (GHz)
Main Geometry	590.97	1.59	14.13	2.74	3.74
Tuning Geometry	471.11	1.61	11.43	2.83	3.62

Table4.18: Best result after tuning procedure for 11mm AK gap case

Peak Output Power (MW)	Output Field Energy (J)	Peak Output Power Efficiency (%)	Energy Efficiency (%)	Frequency (GHz)
476.58	2.33	11.49	4.08	3.69

Table 4.18 gives the best result after the application of tuning procedure. As seen from Table 4.17 and 4.18, energy efficiency is increased from 2.74 % to 4.08%.

4.6.3.2 12m AK Gap Distance

Table 4.19 indicates the results before application of tuning procedure. According to this table; tuning procedure is applied for 3.66 GHz, and the best result after following the procedure is given in Table 4.20 which has the same frequency with natural oscillation frequency. Energy efficiency is increased to 3.58 % from

2.83 % after application of tuning procedure.

Table4.19: Results for 12mm AK gap

	Peak Output Power (MW)	Output Field Energy (J)	Peak Output Power Efficiency (%)	Energy Efficiency (%)	Frequency (GHz)
Main Geometry	509.33	1.44	13.92	2.83	3.77
Tuning Geometry	324.79	0.98	8.94	1.93	3.66

Table4.20: Best result after tuning procedure for 12mm AK gap case

Peak Output Power (MW)	Output Field Energy (J)	Peak Output Power Efficiency (%)	Energy Efficiency (%)	Frequency (GHz)
385.61	1.81	10.50	3.58	3.66

4.6.3.3 13m AK Gap Distance

Table 4.21 shows the results of main and tuning geometry for the case of 13 mm AK gap distance. According to this table, tuning procedure is applied for 3.58 GHz and best result in Table 4.22 with 3.14% energy efficiency at 3.57 GHz operating frequency is obtained. Although this efficiency value is lower than 4.66 % in Table 4.21, it is acceptable because procedure increases the efficiency in the second row in Table 4.21 by giving the desired frequency of oscillation.

Table4.21: Results for 13mm AK gap

	Peak Output Power (MW)	Output Field Energy (J)	Peak Output Power Efficiency (%)	Energy Efficiency (%)	Frequency (GHz)
Main Geometry	526.97	2.13	15.89	4.66	3.03
Tuning Geometry	128.05	0.38	3.89	0.81	3.58

As a conclusion of tuning procedure, it is shown numerically that application of tuning procedure leads to generally enhanced energy efficiency for double gap

Table4.22: Best result after tuning procedure for 13mm AK gap case

Peak Output Power (MW)	Output Field Energy (J)	Peak Output Power Efficiency (%)	Energy Efficiency (%)	Frequency (GHz)
349.48	1.43	10.64	3.14	3.57

viricator. It basically increases the energy efficiency compared to the case of finding natural oscillation frequency because of enabling the internal feedback mechanism.

CHAPTER 5

CONCLUSION AND FUTURE WORK

In order to simulate vircator structures accurately, correct excitation of the coaxial input of device is achieved by using Laplacian option in Magic and result is given in Figure 3.5. Since the input voltage waveform is given to the structure by TEM wave, desired peak voltage value of the input waveform is not observed in simulation due to the reflection of TEM wave from the diode region. In order to correctly determine the peak voltage value of the device, circuit option in Magic is employed and desired waveforms are obtained as in Figure 3.7 and 3.8. After the correct excitation of the signal, anode modeling in Magic is investigated. Grid model and Fraction model is simulated and it is found that fraction entered in Fraction model and geometrical opening of grid model controls the ratio of electron that pass through foil without any deflection as can be seen in Table 3.2. For both models, energy of incident electrons and foil thickness has the same effect on the ratio of forward and backward scattering electrons as indicated in Table 3.3. Besides, higher forward and lower backward scattering ratios are observed in Figure 3.9 when energy of incoming electron beam is increased or thickness of foil is reduced. Furthermore, Table 3.2 shows that effect of material type is included in the foil behavior because of different ratios of forward, backward scattering and capturing electrons are obtained.

Double gap vircator shown in Figure 4.1 is investigated numerically. First, location of VC is verified to be at the output waveguide region for the main geometry. Then, generated mode is found as TE_{10} shown in Figure 4.5 which verifies the expectation when both cutoff frequencies of the device and reasoning explained

in Section 2.2.4. For the operating frequency, mode of the modulating cavity is found as TE_{106} shown in Figure 4.6. After these verifications, beam modulation is mimicked under an applied external signal which causes formation of TE_{106} mode in cavity. Since the delay time caused by oscillations build-up time and feedback to modulation cavity is removed by directly applying of the external signal, earlier start time of microwave generation about 4ns is obtained as shown in Figure 4.11b. However, the reasoning for early termination of the microwave shown in Figure 4.11b for injected signal cases with lower power values couldn't be enlightened clearly. Amplifier concept with virtual cathode devices is already given in [66] and the case of the external signal application which causes microwave generation at the same frequency shows the application of this device as an amplifier with electron beam. Frequency and phase locking ability of double gap vircator are numerically demonstrated in Figure 4.13 and 4.16b respectively which is a sign of ability of this device to be driven by another microwave generator. Effect of cavity field distributions are also tested and the required condition of standing wave maximum point at the beam center for efficient usage of device is demonstrated in Figure 4.18 and Table 4.6. In the case of not satisfying this condition, some other microwave modes of TE_{10p} could be formed in the cavity via feedback window and this results in shifts in frequency of device as indicated in Figure 4.24 and Table 4.11. Cavity field maximum condition leads to another criteria of location of plunger whose distances to beam center must be odd multiples of the quarter of guided wavelength. Every shift of small plunger by half of guided wavelength result in switching of the resonance modes of TE_{10p} as can be seen in Figure 4.22 and Table 4.9. In addition, fine tuning of microwave frequency by using large plunger is demonstrated in Table 4.10. Moreover, periodical dependency of output power to coupling window over every half of guided wavelength given in [62] is obtained in Figure 4.21. Furthermore; as a drawback, dramatic drop of output power due to lower foil transparency values is observed in Table 4.12. From this observation, it is concluded that transparencies especially above 0.95 is required for efficient usage of this structure. By using the observations over effects plungers and coupling window, tuning procedure is developed for double gap vircator with feedback. According to this procedure, natural oscillation frequency is found by employing

the geometry given in Figure 4.26. Then, locations of the plungers are arranged in order to satisfy the condition of standing wave maximum at beam center. After that by using the periodic behavior due to coupling window size, device is optimized. This procedure is applied to 750kV input voltage maximum case, different ak gap distance cases and main geometry for another natural oscillation frequency. As a result, improved energy efficiency values are obtained generally.

As a future work, manufacturing and testing the device in laboratory conditions are considered as the main objective as HPM group in METU. In addition to double gap vircator, corrugated cylindrical waveguide filters could be used as a feedback mechanism to cylindrical axial vircator. One example of this form is given in Ref. [19]. Designing and testing of these filters in the perspective of RF engineering and investigate the effects of S parameter on vircator efficiency might be considered as another future task.

REFERENCES

- [1] S. Champeaux, P. Gouard, R. Cousin, and J. Larour, “3-D PIC Numerical Investigations of a Novel Concept of Multistage Axial Vircator for Enhanced Microwave Generation,” *IEEE Transactions on Plasma Science*, vol. 43, pp. 3841–3855, Nov. 2015.
- [2] B. Goplen, L. Ludeking, D. Smith, and G. Warren, “User-configurable MAGIC for electromagnetic PIC calculations,” *Computer Physics Communications*, vol. 87, pp. 54–86, May 1995.
- [3] L. Ludeking, W. Andrew, and C. Lester, “Magic 3.2.0 Help Manual,” tech. rep., Alliant Techsystems (ATK), Newington, Virginia, Oct. 2011.
- [4] J. Petrén, *Frequency tunability of axial cavity vircators and double anode vircators*. PhD thesis, KTH ROYAL INSTITUTE OF TECHNOLOGY SCHOOL OF ELECTRICAL ENGINEERING, 2016.
- [5] C. S. Hwang, M. W. Wu, P. S. Song, and W. S. Hou, “High power microwave generation from a tunable radially extracted vircator,” *Journal of Applied Physics*, vol. 69, pp. 1247–1252, Feb. 1991.
- [6] S. D. Korovin, S. A. Kitsanov, A. I. Klimov, I. K. Kurkan, I. V. Pegel, S. D. Polevin, V. V. Rostov, and V. P. Tarakanov, “Tunable vircators with e-beam premodulation,” in *PPPS-2001 Pulsed Power Plasma Science 2001. 28th IEEE International Conference on Plasma Science and 13th IEEE International Pulsed Power Conference. Digest of Papers (Cat. No.01CH37251)*, vol. 1, pp. 495–499 vol.1, June 2001.
- [7] S. D. Korovin, I. K. Kurkan, I. V. Pegel, and S. D. Polevin, “Gigawatt S-band frequency-tunable HPM sources,” in *Conference Record of the Twenty-Fifth International Power Modulator Symposium, 2002 and 2002 High-Voltage Workshop.*, pp. 244–247, June 2002.
- [8] C. F. Lynn, J. Parson, P. Kelly, M. Taylor, D. Barnett, A. Neuber, J. Dickens, J. Mankowski, S. Calico, and M. Scott, “Frequency tuning a reflex triode vircator from 1.5 to 5.9 GHz,” in *2014 IEEE International Power Modulator and High Voltage Conference (IPMHVC)*, pp. 209–212, June 2014.

- [9] J. Benford, J. A. Swegle, and E. Schamiloglu, *High Power Microwaves, Third Edition*. Florida: CRC Press, Taylor and Francis Group, 3rd edition ed., 2015.
- [10] H. Sze, D. Price, B. Harteneck, and N. Cooksey, "A master-oscillator-driven phase-locked vircator array," *Journal of Applied Physics*, vol. 68, pp. 3073–3079, Oct. 1990.
- [11] D. Price, H. Sze, and D. Fittinghoff, "Phase and frequency locking of a cavity vircator driven by a relativistic magnetron," *Journal of Applied Physics*, vol. 65, pp. 5185–5189, June 1989.
- [12] D. Price and H. M. Sze, "Phase-stability analysis of the magnetron-driven vircator experiment," *IEEE Transactions on Plasma Science*, vol. 18, pp. 580–585, June 1990.
- [13] W. Woo, J. Benford, D. Fittinghoff, B. Harteneck, D. Price, R. Smith, and H. Sze, "Phase locking of high-power microwave oscillators," *Journal of Applied Physics*, vol. 65, pp. 861–866, Jan. 1989.
- [14] U. Magda and Y. V. Prokopenko, "Co-operative high-power radiation of two beams at the dual vircator complex," in *1996 11th International Conference on High-Power Particle Beams*, vol. 1, pp. 422–425, June 1996.
- [15] A. E. Dubinov, V. D. Selemir, and A. V. Tsarev, "Phased Antenna Arrays Based on Vircators: Numerical Experiments," *Radiophysics and Quantum Electronics*, vol. 43, pp. 637–642, Aug. 2000.
- [16] K. J. Hendricks, R. Adler, and R. C. Noggle, "Experimental results of phase locking two virtual cathode oscillators," *Journal of Applied Physics*, vol. 68, pp. 820–825, July 1990.
- [17] H. Sze, D. Price, and B. Harteneck, "Phase locking of two strongly coupled vircators," *Journal of Applied Physics*, vol. 67, pp. 2278–2282, Mar. 1990.
- [18] S. Champeaux, P. Gouard, R. Cousin, and J. Larour, "Improved Design of a Multistage Axial Vircator With Reflectors for Enhanced Performances," *IEEE Transactions on Plasma Science*, vol. 44, pp. 31–38, Jan. 2016.
- [19] L. Zhi-Qiang, Z. Hui-Huang, F. Yu-Wei, S. Ting, Y. Jian-Hua, Y. Cheng-Wei, X. Liu-Rong, and Z. Yan-Song, "Simulation and Experimental Research of a Novel Vircator," *Chinese Physics Letters*, vol. 25, pp. 2566–2568, July 2008.
- [20] J. Benford, D. Price, H. Sze, and D. Bromley, "Interaction of a vircator microwave generator with an enclosing resonant cavity," *Journal of Applied Physics*, vol. 61, pp. 2098–2100, Mar. 1987.

- [21] W. Jiang, N. Shimada, S. Prasad, and K. Yatsui, "Experimental and Simulation Studies of New Configuration of Virtual Cathode Oscillator," *IEEE Transactions on Plasma Science*, vol. 32, pp. 54–59, Feb. 2004.
- [22] D. Shiffler, M. LaCour, K. Golby, M. Sena, M. Mithcell, M. Haworth, K. Hendricks, and T. Spencer, "Comparison of velvet-and cesium iodide-coated carbon fiber cathodes," *IEEE Transactions on plasma science*, vol. 29, no. 3, pp. 445–451, 2001.
- [23] L. Liu, L.-M. Li, X.-P. Zhang, J.-C. Wen, H. Wan, and Y.-Z. Zhang, "Efficiency Enhancement of Reflex Triode Virtual Cathode Oscillator Using the Carbon Fiber Cathode," *IEEE Transactions on Plasma Science*, vol. 35, pp. 361–368, Apr. 2007.
- [24] Y. Chen, J. Mankowski, J. Walter, M. Kristiansen, and R. Gale, "Cathode and anode optimization in a virtual cathode oscillator," *IEEE Transactions on Dielectrics and Electrical Insulation*, vol. 14, no. 4, 2007.
- [25] M. Elfsberg, T. Hurtig, A. Larsson, C. Moller, and S. Nyholm, "Experimental Studies of Anode and Cathode Materials in a Repetitive Driven Axial Vircator," *IEEE Transactions on Plasma Science*, vol. 36, pp. 688–693, June 2008.
- [26] J. Ju, D. Cai, G. Du, Y. Wang, L. Liu, and J. Zhang, "Characterization of Cesium Iodide-Coated Carbon-Fiber Aluminum Cathode for an S -Band High-Efficiency Vircator," *IEEE Transactions on Plasma Science*, vol. 43, pp. 3522–3526, Oct. 2015.
- [27] C. F. Lynn, J. M. Parson, M. C. Scott, S. E. Calico, J. C. Dickens, A. A. Neuber, and J. J. Mankowski, "Anode Materials for High-Average-Power Operation in Vacuum at Gigawatt Instantaneous Power Levels," *IEEE Transactions on Electron Devices*, vol. 62, pp. 2044–2047, June 2015.
- [28] A. M. Efremov, A. A. Zherlitsyn, S. A. Kitsanov, A. I. Klimov, S. D. Korovin, B. M. Koval'chuk, I. K. Kurkan, O. P. Kutenkov, S. V. Loginov, I. V. Pegel', and S. D. Polevin, "An S-band vircator with premodulated electron beam based on a compact generator with inductive energy storage," *Technical Physics Letters*, vol. 27, pp. 289–291, Apr. 2001.
- [29] S. A. Kitsanov, A. I. Klimov, S. D. Korovin, I. K. Kurkan, I. V. Pegel, and S. D. Polevin, "Vircator with electron beam premodulation built around a high-current pulsed-periodic accelerator," *Technical Physics*, vol. 47, no. 5, pp. 595–603, 2002.
- [30] C. Möller, F. Bieth, P. Delmote, M. Elfsberg, T. Hurtig, and S. E. Nyholm, "Experimental study of a vircator with premodulated electron beam," in *Pulsed Power Conference (PPC), 2011 IEEE*, pp. 815–818, IEEE, 2011.

- [31] P. V. Molchanov, E. A. Gurnevich, V. V. Tikhomirov, and S. E. Siahlo, "Simulation of an axial vircator with a three-cavity resonator," *arXiv:1408.1824 [physics]*, Aug. 2014. arXiv: 1408.1824.
- [32] R. B. Miller, *An Introduction to the Physics of Intense Charged Particle Beams*. Plenum Press, 1982. OCLC: 861212282.
- [33] K. S. Woolverton, *High-power, coaxial vircator geometries*. PhD thesis, Texas Tech University, 1998.
- [34] S. Pai and Q. Zhang, *Introduction to High Power Pulse Technology*. Singapore: World Scientific Publishing Co. Pte. Ltd., 1995.
- [35] S. Humphries, *Charged particle beams*. A Wiley-Interscience publication, New York: Wiley, 1990.
- [36] L. Li, G. Cheng, L. Zhang, X. Ji, L. Chang, Q. Xu, L. Liu, J. Wen, C. Li, and H. Wan, "Role of the rise rate of beam current in the microwave radiation of vircator," *Journal of Applied Physics*, vol. 109, p. 074504, Apr. 2011.
- [37] M. Yatsuzuka, M. Nakayama, S. Nobuhara, D. Young, and O. Ishihara, "Effect of plasma formation on electron pinching and microwave emission in a virtual cathode oscillator," in *1996 11th International Conference on High-Power Particle Beams*, vol. 1, pp. 481–484, June 1996.
- [38] D. T. Young, *Effects of diode gap closure and bipolar flow on vircator microwave generation*. PhD thesis, Texas Tech University, 1996.
- [39] D. J. Sullivan, J. E. Walsh, and E. A. Coutsiias, "Virtual cathode oscillator (vircator) theory," in *High-Power Microwave Sources* (V. L. Granatstein and I. Alexeff, eds.), Artech House Publishers, 1987.
- [40] C. D. Child, "Discharge from hot CaO," *Physical Review (Series I)*, vol. 32, no. 5, p. 492, 1911.
- [41] I. Langmuir, "The effect of space charge and residual gases on thermionic currents in high vacuum," *Physical Review*, vol. 2, no. 6, p. 450, 1913.
- [42] H. R. Jory and A. W. Trivelpiece, "Exact Relativistic Solution for the One-Dimensional Diode," *Journal of Applied Physics*, vol. 40, pp. 3924–3926, Sept. 1969.
- [43] T. J. T. Kwan and L. E. Thode, "Formation of virtual cathodes and microwave generation in relativistic electron beams," *Physics of Fluids*, vol. 27, no. 7, p. 1570, 1984.
- [44] R. A. Mahaffey, P. Sprangle, J. Golden, and C. A. Kapetanacos, "High-power microwaves from a nonisochronic reflecting electron system," *Physical Review Letters*, vol. 39, no. 13, p. 843, 1977.

- [45] E.-H. Choi, M.-C. Choi, Y. Jung, M.-W. Choug, J.-J. Ko, Y. Seo, G. Cho, H. S. Uhm, and H. Suk, “High-power microwave generation from an axially extracted virtual cathode oscillator,” *IEEE Transactions on Plasma Science*, vol. 28, pp. 2128–2134, Dec. 2000.
- [46] T. J. T. Kwan, “High-power coherent microwave generation from oscillating virtual cathodes,” *Physics of Fluids*, vol. 27, no. 1, p. 228, 1984.
- [47] B. V. Alyokhin, A. E. Dubinov, V. D. Selemir, O. A. Shamro, K. V. Shibalko, N. V. Stepanov, and V. E. Vatrugin, “Theoretical and experimental studies of virtual cathode microwave devices,” *IEEE Transactions on Plasma Science*, vol. 22, pp. 945–959, Oct. 1994.
- [48] M. Haworth, R. Adler, B. Anderson, M. Connaughton, W. Dungan, J. Enns, J. Metz, P. Pelletier, R. Platt, J. Polaco, R. Rupp, L. Thode, and D. Voss, “Experimental observation of two microwave radiation mechanisms with widely separated frequencies during the output pulse of a high-voltage virtual cathode oscillator,” *Applied Physics Letters*, vol. 59, pp. 408–410, July 1991.
- [49] D. J. Sullivan, “High Power Microwave Generation from a Virtual Cathode Oscillator (Viricator),” *IEEE Transactions on Nuclear Science*, vol. 30, pp. 3426–3428, Aug. 1983.
- [50] P. Poulsen, P. A. Pincosy, and J. J. Morrison, “Progress toward steady-state high-efficiency viricators,” in *Intense Microwave and Particle Beams II*, vol. 1407, pp. 172–183, International Society for Optics and Photonics, Apr. 1991.
- [51] T. J. T. Kwan and H. A. Davis, “Numerical Simulations of the Reditron,” *IEEE Transactions on Plasma Science*, vol. 16, pp. 185–191, Apr. 1988.
- [52] H. A. Davis, R. R. Bartsch, T. J. T. Kwan, E. G. Sherwood, and R. M. Stringfield, “Experimental confirmation of the reditron concept,” *IEEE Transactions on Plasma Science*, vol. 16, pp. 192–198, Apr. 1988.
- [53] H. Sze, J. Benford, T. Young, D. Bromley, and B. Harteneck, “A Radially and Axially Extracted Virtual-Cathode Oscillator (Viricator),” *IEEE Transactions on Plasma Science*, vol. 13, pp. 492–497, Dec. 1985.
- [54] S. D. Korovin, I. V. Pegel, S. D. Polevin, and V. P. Tarakanov, “Numerical simulation of efficient 1.5 GHz viricator,” in *Digest of Technical Papers. 11th IEEE International Pulsed Power Conference (Cat. No.97CH36127)*, vol. 1, pp. 736–741 vol.1, June 1997.
- [55] V. S. Voronin, Y. T. Zozulya, and A. N. Lebedev, “Self-consistent stationary of a relativistic electron beam in drift space,” *Soviet Physics. Technical Physics*, vol. 17, pp. 432–436, 1972.

- [56] A. S. Shlapakovski, T. Queller, Y. P. Bliokh, and Y. E. Krasik, “Investigations of a Double-Gap Vircator at Submicrosecond Pulse Durations,” *IEEE Transactions on Plasma Science*, vol. 40, pp. 1607–1617, June 2012.
- [57] A. E. Dubinov and V. D. Selemir, “Vircator generation spectrum controlled by an external SHF signal,” *Technical Physics Letters*, vol. 26, no. 7, pp. 547–549, 2000.
- [58] S. A. Kitsanov, A. I. Klimov, S. D. Korovin, I. K. Kurkan, O. P. Kutenkov, I. V. Pegel, S. D. Polevin, V. V. Rostov, V. P. Tarakanov, and R. Wioland, “Tunable L-band and S-band gigawatt vircators with feedback,” in *2000 13th International Conference on High-Power Particle Beams*, pp. 726–729, June 2000.
- [59] S. A. Kitsanov, A. I. Klimov, S. D. Korovin, B. M. Kovalchuk, I. K. Kurkan, S. V. Loginov, I. V. Pegel, S. D. Polevin, S. N. Volkov, and A. A. Zherlitsyn, “S-band vircator with electron beam premodulation based on compact pulse driver with inductive energy storage,” *IEEE Transactions on Plasma Science*, vol. 30, pp. 1179–1185, June 2002.
- [60] S. D. Polevin, S. A. Kitsanov, S. D. Korovin, B. M. Kovalchuk, I. K. Kurkan, S. V. Loginov, I. V. Pegel, S. N. Volkov, and A. A. Zherlitsyn, “Spontaneous pulse width limitation in S-band two-sectional vircator,” in *High-Power Particle Beams (BEAMS 2004), 2004 International Conference on*, pp. 483–486, IEEE, 2004.
- [61] B. V. Alekhin, V. V. Voronin, S. L. Voronov, O. I. Kovalenko, S. S. Pavlov, V. D. Selemir, N. V. Stepanov, V. G. Suvorov, and V. D. Suryakov, “Effective pulsed-repetitive vircator with double anode grid,” in *2004 International Conference on High-Power Particle Beams (BEAMS 2004)*, pp. 544–547, July 2004.
- [62] H. Wang and Y. Zhang, “A virtual cathode oscillator with double cavities,” in *Pulsed Power Conference, 2007 16th IEEE International*, vol. 1, pp. 784–787, IEEE, 2007.
- [63] A. S. Shlapakovski, T. Queller, Y. Hadas, Y. E. Krasik, S. D. Polevin, and I. K. Kurkan, “Effects of Different Cathode Materials on Submicrosecond Double-Gap Vircator Operation,” *IEEE Transactions on Plasma Science*, vol. 37, pp. 1233–1241, July 2009.
- [64] T. Queller, A. Shlapakovski, and Y. E. Krasik, “Plasma formation in a double-gap vircator,” *Journal of Applied Physics*, vol. 108, p. 103302, Nov. 2010.
- [65] B. M. Kovalchuk, S. D. Polevin, R. V. Tsygankov, and A. A. Zherlitsyn, “S-Band Coaxial Vircator With Electron Beam Premodulation Based on

- Compact Linear Transformer Driver,” *IEEE Transactions on Plasma Science*, vol. 38, pp. 2819–2824, Oct. 2010.
- [66] S. A. Kurkin, N. S. Frolov, A. O. Rak, A. A. Koronovskii, A. A. Kuraev, and A. E. Hramov, “High-power microwave amplifier based on overcritical relativistic electron beam without external magnetic field,” *Applied Physics Letters*, vol. 106, no. 15, p. 153503, 2015.
- [67] A. N. Didenko, M. Y. Antoshkin, G. P. Fomenko, V. P. Grigoryev, T. V. Koval, G. V. Melnikov, V. I. Tsvetkov, and A. G. Zherlitsin, “Frequency control of vircators microwave radiation,” in *1992 9th International Conference on High-Power Particle Beams*, vol. 3, pp. 1690–1695, May 1992.
- [68] M. V. Fazio, J. Kinross-Wright, B. Haynes, and R. F. Hoeberling, “The virtual cathode microwave amplifier experiment,” *Journal of Applied Physics*, vol. 66, pp. 2675–2677, Sept. 1989.
- [69] Y. A. Kalinin, A. V. Starodubov, and A. S. Fokin, “An experimental study of the interaction between a pulsed electron beam and a large-amplitude electromagnetic wave,” *Technical Physics Letters*, vol. 41, pp. 40–42, Jan. 2015.
- [70] N. Phrolov, A. Koronovskii, Y. Kalinin, S. Kurkin, A. Starodubov, and A. Hramov, “The effect of an external signal on output microwave power of a low-voltage vircator,” *Physics Letters A*, vol. 378, pp. 2423–2428, June 2014.
- [71] N. S. Frolov, A. A. Koronovskii, A. E. Hramov, Y. A. Kalinin, and A. V. Starodubov, “Theoretical and experimental analysis of the microwave radiation power of a generator on a virtual cathode subjected to external harmonic exposure,” *Bulletin of the Russian Academy of Sciences: Physics*, vol. 76, pp. 1329–1332, Dec. 2012.
- [72] W.-y. Woo, “Two-dimensional features of virtual cathode and microwave emission,” *Physics of Fluids*, vol. 30, no. 1, p. 239, 1987.
- [73] L. Zhenxiang, S. Ting, Z. Jiande, and Q. Baoliang, “Particle Simulation of an Improved Axially Extracted Vircator,” *Plasma Science and Technology*, vol. 5, pp. 2007–2010, Oct. 2003.
- [74] W. Jeon, J. E. Lim, M. W. Moon, K. B. Jung, W. B. Park, H. M. Shin, Y. Seo, and E. H. Choi, “Output characteristics of the high-power microwave generated from a coaxial vircator with a bar reflector in a drift region,” *IEEE Transactions on Plasma Science*, vol. 34, pp. 937–944, June 2006.
- [75] S. Ting, W. Yong, Q. Bao-Liang, and T. Qi-Mei, “A Compact Vircator with Feedback Annulus Operated in Quasi-Single TM_{01} Mode Within the C Band,” *Chinese Physics Letters*, vol. 19, pp. 1646–1648, Nov. 2002.

- [76] Y.-W. Fan, Z.-Q. Li, T. Shu, and J. Liu, “Efficiency and stability enhancement of a virtual cathode oscillator,” *Chinese Physics B*, vol. 23, p. 075208, July 2014.
- [77] E. Gurnevich and P. Molchanov, “The Effect of the Electron-Beam Parameter Spread on Microwave Generation in a Three-Cavity Axial Vircator,” *IEEE Transactions on Plasma Science*, vol. 43, pp. 1014–1017, Apr. 2015.
- [78] V. Baryshevsky, A. Gurinovich, E. Gurnevich, and P. Molchanov, “Experimental Study of an Axial Vircator With Resonant Cavity,” *IEEE Transactions on Plasma Science*, vol. 43, pp. 3507–3511, Oct. 2015.
- [79] G. Singh and S. Chaturvedi, “PIC simulation of effect of energy-dependent foil transparency in an axially-extracted vircator,” *IEEE Transactions on Plasma Science*, vol. 32, pp. 2210–2216, Dec. 2004.
- [80] G. Singh and S. Chaturvedi, “Particle-in-cell simulations for virtual cathode oscillator including foil ablation effects,” *Physics of Plasmas*, vol. 18, p. 063104, June 2011.
- [81] Y.-J. Chen, J. Mankowski, J. Walter, and M. Kristiansen, “Virtual Cathode Oscillator Component Optimization,” in *Power Modulator Symposium, 2006. Conference Record of the 2006 Twenty-Seventh International*, pp. 157–160, IEEE, 2006.
- [82] V. Baryshevsky, A. Gurinovich, E. Gurnevich, and P. Molchanov, “Experimental Study of a Triode Reflex Geometry Vircator,” *IEEE Transactions on Plasma Science*, vol. 45, pp. 631–635, Apr. 2017.
- [83] S. A. Kitsanov, A. I. Klimov, S. D. Korovin, I. K. Kurkan, I. V. Pegel, and S. D. Polevin, “A vircator with electron beam premodulation based on high-current repetitively pulsed accelerator,” *IEEE Transactions on Plasma Science*, vol. 30, pp. 274–285, Feb. 2002.